Monthly Notices
of the
ROYAL ASTRONOMICAL SOCIETY

MNRAS **512,** 2654–2668 (2022)
Advance Access publication 2022 March 12
https://doi.org/10.1093/mnras/stac685

Host galaxies and electromagnetic counterparts to binary neutron star mergers across the cosmic time: detectability of GW170817-like events

Rosalba Perna,[1,2]★ M. Celeste Artale ,[3,4,5] Yi-Han Wang ,[1] Michela Mapelli,[5,6,7] Davide Lazzati ,[8] Cecilia Sgalletta[5,9] and Filippo Santoliquido[5,6]

[1] *Department of Physics and Astronomy, Stony Brook University, Stony Brook, NY 11794, USA*
[2] *Center for Computational Astrophysics, Flatiron Institute, 162 5th Avenue, New York, NY 10010, USA*
[3] *Institut für Astro- und Teilchenphysik, Universität Innsbruck, Technikerstrasse 25/8, A-6020, Innsbruck, Austria*
[4] *Department of Physics and Astronomy, Purdue University, 525 Northwestern Avenue, West Lafayette, IN 47907, USA*
[5] *Physics and Astronomy Department Galileo Galilei, University of Padova, Vicolo dell'Osservatorio 3, I-35122, Padova, Italy*
[6] *INFN - Padova, Via Marzolo 8, I-35131, Padova, Italy*
[7] *INAF - Osservatorio Astronomico di Padova, Vicolo dell'Osservatorio 5, I-35122, Padova, Italy*
[8] *Department of Physics, Oregon State University, 301 Weniger Hall, Corvallis, OR 97331, USA*
[9] *SISSA, via Bonomea 265, I-34136, Trieste, Italy*

Accepted 2022 March 9. Received 2022 March 5; in original form 2021 December 8

ABSTRACT

The association of GRB170817A with a binary neutron star (BNS) merger has revealed that BNSs produce at least a fraction of short gamma-ray bursts (SGRBs). As gravitational wave (GW) detectors push their horizons, it is important to assess coupled electromagnetic (EM)/GW probabilities and maximize observational prospects. Here, we perform BNS population synthesis calculations with the code `MOBSE`, seeding the binaries in galaxies at three representative redshifts, $z = 0.01$, 0.1, and 1 of the Illustris TNG50 simulation. The binaries are evolved and their locations numerically tracked in the host galactic potentials until merger. Adopting the microphysics parameters of GRB170817A, we numerically compute the broad-band light curves of jets from BNS mergers, with the afterglow brightness dependent on the local medium density at the merger site. We perform Monte Carlo simulations of the resulting EM population assuming either a random viewing angle with respect to the jet, or a jet aligned with the orbital angular momentum of the binary, which biases the viewing angle probability for GW-triggered events. We find a gamma-ray detection probability of ~ 2 per cent, 10 per cent, and 40 per cent for BNSs at $z = 1$, 0.1, and 0.01, respectively, for the random case, rising to ~ 75 per cent for the $z = 0.01$, GW-triggered aligned case. Afterglow detection probabilities of GW-triggered BNS mergers vary in the range of ~ 0.3–0.5 per cent, with higher values for aligned jets, and are comparable across the high- and low-energy bands, unlike gamma-ray-triggered events (cosmological SGRBs) which are significantly brighter at higher energies. We further quantify observational biases with respect to host galaxy masses.

Key words: galaxies: general – *(stars:)* binaries *(including multiple)*: close – *(stars:)* gamma-ray burst: general.

1 INTRODUCTION

The almost simultaneous detection of gravitational waves (GWs) and broad-band photons (gamma-rays through radio) from a binary neutron star (BNS) merger was a historical event Abbott et al. (2017c). It heralded the new age of multimessenger astrophysics, an era in which the combination of different messengers (in this case GWs and photons) gives information about a source that could have not otherwise been revealed without the multimessenger synergy (Alexander et al. 2017, 2018; Haggard et al. 2017; Hallinan et al. 2017; Kasliwal et al. 2017; Margutti et al. 2017, 2018; Troja et al. 2017; Dobie et al. 2018; Lyman et al. 2018; Resmi et al. 2018; Ruan et al. 2018; Lamb et al. 2019; Piro et al. 2019).

Understanding the astrophysical origin of the binary mergers detected by LIGO–Virgo is of much interest, and deeply connected to the environments in which these events occur. Events in galactic fields are more likely associated with compact object (CO) binaries formed via stellar evolution from binary stars (e.g. Tutukov & Yungelson 1973; Portegies Zwart & Yungelson 1998; Belczynski, Kalogera & Bulik 2002; Voss & Tauris 2003; Podsiadlowski et al. 2004; Belczynski et al. 2007, 2017, 2018; Belczynski et al. 2016; de Mink & Mandel 2016; Eldridge & Stanway 2016; Marchant et al. 2016; Stevenson, Berry & Mandel 2017; Giacobbo, Mapelli & Spera 2018; Vigna-Gómez et al. 2018; Spera et al. 2019; Tanikawa et al. 2021), whereas mergers in globular clusters (e.g. Portegies Zwart & McMillan 2000; Downing et al. 2010; Samsing, MacLeod & Ramirez-Ruiz 2014; Rodriguez et al. 2015; Antonini et al. 2016; Rodriguez, Chatterjee & Rasio 2016; Askar et al. 2017; Rodriguez & Loeb 2018; Samsing 2018; Fragione et al. 2019a; Fragione, Leigh & Perna 2019b; Fragione & Loeb 2019; Zevin et al. 2019; Antonini & Gieles 2020; Fragione & Silk 2020; Mapelli et al. 2021), young star clusters (e.g. Banerjee, Baumgardt & Kroupa 2010; Ziosi et al. 2014; Mapelli 2016; Banerjee 2017, 2021; Di Carlo et al. 2019,

---

★ E-mail: rosalba.perna@stonybrook.edu

© 2022 The Author(s)
Published by Oxford University Press on behalf of Royal Astronomical Society

Downloaded from https://academic.oup.com/mnras/article/512/2/2654/6547794 by libraryerms@stonybrook.edu user on 05 April 2022

2020a, 2020b; Kumamoto, Fujii & Tanikawa 2019; Perna et al. 2019; Kremer et al. 2020; Rastello et al. 2020; Santoliquido et al. 2020), or discs of active galactic nuclei (AGNs, e.g. O'Leary et al. 2006; Miller & Lauburg 2009; McKernan et al. 2012; Antonini & Rasio 2016; Bartos et al. 2017; Stone, Metzger & Haiman 2017; McKernan et al. 2018; Rasskazov & Kocsis 2019; Yang et al. 2019a, b; Arca Sedda 2020; Arca Sedda et al. 2020; Tagawa, Haiman & Kocsis 2020a, b; Perna, Lazzati & Cantiello 2021a; Perna et al. 2021b; Tagawa et al. 2021a, b; Zhu et al. 2021) are dominated by binaries formed via dynamical interactions. In addition to providing important clues on the formation channels of the CO binaries, host galaxy identification is key in order to measure the Hubble constant (Abbott et al. 2017b; Palmese et al. 2020).

Observational and theoretical studies of the host galaxies of binary COs pre-date the detection of GWs (e.g. Perna & Belczynski 2002; Bloom 2003; Voss & Tauris 2003; Fan et al. 2005; Belczynski et al. 2006; Covino et al. 2006; Nakar, Gal-Yam & Fox 2006; O'Shaughnessy, Belczynski & Kalogera 2008; Piranomonte et al. 2008; Antonelli et al. 2009; D'Avanzo et al. 2009; Guetta & Stella 2009; Berger 2010; Kopač et al. 2012; Margutti et al. 2012; Fong & Berger 2013; Fong et al. 2015). Since the short gamma-ray bursts (SGRBs) have long been suspected to be associated with BNS and neutron star–black hole (NSBH) mergers, studies of the galaxy hosts have provided remarkable clues on to the evolutionary channels leading to the observed SGRBs. Events occurring in elliptical galaxies are more likely associated with binaries merging after a long delay time, whereas associations with star-forming regions in spiral and starburst galaxies indicate a more prompt merger.

Since the detection of GWs from merging COs, there has been a revival of host galaxy studies to further understand the astrophysical origin of the detected events, especially when an electromagnetic (EM) counterpart accompanies the GW detection. Most recent works have moved beyond the use of semi-analytical models of galaxy population, and rather used galaxy catalogues generated from large-scale numerical simulations, which have been coupled with the results of population synthesis calculations of binary evolution. This has allowed to explore in better detail the dependence of binary mergers of different types of COs on properties of their host galaxies such as the stellar mass, star-formation rate, metallicity, and colours (Cao, Lu & Zhao 2018; Adhikari et al. 2020; Perets & Beniamini 2021; Rose et al. 2021; Chu, Yu & Lu 2022). Mapelli & Giacobbo (2018), drawing upon galaxies from the cosmological box Illustris-1 (Vogelsberger et al. 2013), found that BNS mergers tend to form and merge in galaxies with stellar mass $\sim 10^9$–10^{12} $\mathrm{M}_\odot$, while NSBH and binary black holes preferentially form in lower mass galaxies ($<10^{10}$ $\mathrm{M}_\odot$) but a fraction of them merge in more massive galaxies due to the longer time delays. Artale et al. (2019, 2020a), using galaxy renderings from the EAGLE simulation (Schaye et al. 2015), found that, for all types of CO mergers and for a wide range of redshifts between 0 and 6, there is a strong correlation between the binary merger rate and the stellar mass of the host galaxy. They further found that at low redshift early-type galaxies give a larger contribution to the merger rate density than late-type galaxies, while the trend reverses at redshifts higher than about 1.

In order to be able to compare the results of simulations with actual data, and hence verify/dispute/discriminate among various CO models, it is of paramount importance to understand whether the population of electromagnetically detected CO mergers, which is the one allowing host galaxy identification, is biased with respect to the underlying merging population. The longer wavelength afterglow radiation following the prompt gamma-rays, which is key to galaxy association, depends on the density of gas in the medium. Hence, galaxies of different masses, and different merger locations within the same galaxy, will produce different brightness for the afterglow radiation, even for similar intrinsic properties of the source (that is jet energetics, microphysical parameters associated with the afterglow emission, and viewing angle with respect to the observer). Whether this may result in a bias of the galaxy-detected BNS population (and, if so, by what extent), is an open question which we address in this work.

More specifically, here we couple the computation of stellar binaries leading to BNS mergers performed with the code MOBSE (Giacobbo et al. 2018), with the galaxy catalogue from the Illustris TNG50 simulation (Pillepich et al. 2019), and state-of-the-art numerical modelling of the afterglow radiation from BNS mergers (Lazzati et al. 2018), to predict the broad-band emission properties of the BNS merging population, for three representative redshifts ($z = 0.01$, 0.1, and 1), and for a range of galaxy masses. We predict the fraction of BNS mergers expected to yield detectable radiation in various representative bands, and we investigate the extent to which the observable population is biased with respect to the intrinsic sample. Our paper is organized as follows: In Section 2, we summarize the various ingredients of the modelling; Section 3 describes the results of the simulated population of EM sources, and analyses biases with respect to the intrinsic one. We summarize in Section 4.

2 METHODS

2.1 Population synthesis calculations of binary stars leading to BNS mergers

As discussed in the introduction, binary COs, and in particular BNSs of interest here, can form via a variety of formation channels, which are favoured in different environments. In this work, we specifically focus on BNS systems formed from isolated binary star evolution via common envelope.

The evolution of stars in binary systems, and hence the properties of BNSs at the time of mergers, have been the subject of numerous investigations using population synthesis codes (e.g. Tutukov & Yungelson 1973; Portegies Zwart & Yungelson 1998; Bloom, Sigurdsson & Pols 1999; Belczynski et al. 2002, 2007, 2016, 2017; Voss & Tauris 2003; Podsiadlowski et al. 2004; O'Shaughnessy, Kalogera & Belczynski 2010; de Mink & Mandel 2016; Eldridge & Stanway 2016; Marchant et al. 2016; Stevenson et al. 2017; Giacobbo et al. 2018; Mapelli & Giacobbo 2018; Vigna-Gómez et al. 2018; Neijssel et al. 2019; Tang et al. 2020; Mandel & Broekgaarden 2021; Tanikawa et al. 2021), coupled with either semi-analytical prescriptions for galaxy modelling and evolution (e.g. Perna & Belczynski 2002; Belczynski et al. 2006), or with results from numerical simulations of galaxy formation (e.g. Artale et al. 2019, 2020a, b; Briel et al. 2021; Mandhai et al. 2021; Chu et al. 2022). The predicted global rates suffer from rather large uncertainties due to a combination of not-well-constrained model inputs (i.e. the initial mass function, the metallicity and its cosmic evolution, the star-formation rate, and the natal kick prescription), and the physics of common envelope evolution (e.g. Dominik et al. 2013; Chruslinska et al. 2018; Mapelli & Giacobbo 2018; Chruslinska, Nelemans & Belczynski 2019; Santoliquido et al. 2021). In this work, to minimize the influence on our results from the uncertain, redshift-dependent input parameters, we focus on selected representative redshifts slices, and on the statistical properties of the galaxies at those redshifts as derived from state-of-the-art cosmological simulations (Section 2.3).

Isolated binary evolution is modelled using the population synthesis code MOBSE (Giacobbo et al. 2018). In the following we

Downloaded from https://academic.oup.com/mnras/article/512/2/2654/6547794 by libraryerms@stonybrook.edu user on 05 April 2022

summarize the key elements and assumptions of this code, while more details can be found in the papers cited above. The mass-loss rate of a massive hot star of metalllicity Z is modelled according to the prescription $\dot{M} \propto Z^{\beta}$, where β is a parameter dependent on the Eddington ratio (Giacobbo et al. 2018). The initial mass function follows the Kroupa law (Kroupa 2001) in the high mass range, that is $\mathrm{d}N/\mathrm{d}M \propto M^{-2.3}$. The orbital periods, eccentricities, and mass ratios of the massive binary stars are drawn from Sana et al. (2012), yielding the distribution $\mathcal{F}(q) \propto q^{-0.1}$ with $q \in [0.1\text{–}1]$ for the mass ratio $q = m_2/m_1$; the orbital period P is drawn from $\mathcal{F}(\Pi) \propto \Pi^{-0.55}$ with $\Pi = \log{(P/\mathrm{d})} \in [0.15\text{–}5.5]$ and the eccentricity e from $\mathcal{F}(e) \propto e^{-0.42}$ with $0 \leq e \leq 0.9$.

The metallicity distribution comes directly from the Illustris TNG50 simulation. Our simulation grid with MOBSE has 12 values of metallicity between $Z = 0.0002$ and $Z = 0.02$. Mass transfer via Roche lobe overflow is modelled according to the prescription of Hurley, Tout & Pols (2002), yielding a nearly conservative mass transfer if the accretor is a non-degenerate star.

The assumed functional form of the neutron star (NS) kick distribution is

$$v_{\rm kick} = f_{\rm H05}\,\frac{m_{\rm ej}}{\langle m_{\rm ej}\rangle}\,\frac{\langle m_{\rm NS}\rangle}{m_{\rm rem}}, \qquad (1)$$

where $m_{\rm ej}$ is the mass of the ejecta, $m_{\rm rem}$ is the mass of the compact remnant, $\langle m_{\rm NS}\rangle$ is the average NS mass, and $\langle m_{\rm ej}\rangle$ is the average mass of the ejecta associated with the formation of a NS of mass $\langle m_{\rm NS}\rangle$ from single stellar evolution. Finally, $f_{\rm H05}$ is a random value extracted from a Maxwellian distribution with one-dimensional root mean square $\sigma_{\rm 1D} = 265\ \mathrm{km\,s^{-1}}$. We use a Maxwellian distribution with $\sigma_{\rm 1D} = 265\ \mathrm{km\,s^{-1}}$ because this matches the proper motions of young pulsars in the Milky Way[1] (Hobbs et al. 2005). We refer to Giacobbo & Mapelli (2020) for more detail on the kick model.

2.2 Mergers in host galaxies from the Illustris TNG50 simulation

The host galaxies of binary COs are selected from the cosmological magnetohydrodynamical simulation TNG50 (Marinacci et al. 2018; Naiman et al. 2018; Nelson et al. 2018, 2019a, b; Pillepich et al. 2018a, b, 2019; Springel et al. 2018), the third and final of the IllustrisTNG project. TNG50 initially contains 2160^3 dark matter particles and the same number in gas cells in a volume of $(50\,\mathrm{Mpc})^3$. It has an average spatial resolution of ~70–140 pc, and is able to resolve baryonic masses down to $8.5 \times 10^4\ \mathrm{M}_{\odot}$. The simulation includes several key elements of subgrid physics, such as star formation, cooling, supernova and AGN feedback, accretion and mergers, and formation of supermassive black holes (Vogelsberger et al. 2013; Pillepich et al. 2018a). At a redshift of 1, Illustris TNG50 samples about 6500 galaxies with stellar mass larger than $10^8\ \mathrm{M}_{\odot}$ at an unparalleled level of detail, resolving internal structure of galaxies and providing insight into their chemo-dynamical evolution. The simulation spans a large swath of cosmic history, from very high redshifts to the present time. The initial conditions of the simulation series have been created at $z = 127$. In this work, we focus on three redshift snapshots: $z = 0.01$, 0.1, and 1. These encompass the range in which (at least the brightest) EM counterparts from SGRBs can be detected, while the lowest redshift, corresponding to a distance of ~45 Mpc, is within the current LIGO–Virgo horizon. Analysis of the simulated EM counterparts at this redshift will allow us to evaluate the probability of detecting an EM counterpart to a GW-detected BNS merger.

The catalogues of merging BNSs are coupled with the galaxies in the Illustris TNG50 simulation following the formalism developed by Mapelli et al. (2017). The MOBSE simulations provide, for each binary system which merges in less than the Hubble time, the NS masses and the delay time $t_{\rm delay}$ between the formation of the progenitor stars and the BNS merger. For a given stellar mass particle $M_{\rm TNG50}$ formed at a redshift $z_{\rm TNG50}$ and with metallicity $Z_{\rm TNG50}$ in the Illustris TNG50 simulation, we associate a number $n_{\rm BNS}$ of BNSs from progenitors stars with the closest metallicity to the MOBSE tables ($Z_{\rm TNG50} \sim Z_{\rm BSE}$) as

$$n_{\rm BNS} = N_{\rm BSE}\,\frac{M_{\rm TNG50}}{M_{\rm BSE}}\,f_{\rm corr}\,f_{\rm bin}. \qquad (2)$$

Here, $N_{\rm BSE}$ is the number of merging BNS within the simulated subset of initial stellar mass $M_{\rm BSE}$ with MOBSE, $f_{\rm bin} = 0.4$ is the assumed fraction of stellar mass in binaries, and $f_{\rm corr} = 0.285$ corrects for the fact that only binaries with primary mass larger than 5 $\mathrm{M}_{\odot}$ are simulated. The correction factor $f_{\rm corr}$ is calculated assuming that the universal initial mass function of stars is described as in Kroupa (2001), and corresponds to the fraction of the total initial stellar mass that we expect in stars with mass $\in [0.1, 5]\ \mathrm{M}_{\odot}$. A binary fraction $f_{\rm bin} = 0.4$ is the observed binary fraction in the local Universe integrated across all possible stellar masses (Moe & Di Stefano 2017). The lookback time of the merging BNSs in the Monte Carlo selected sample, $t_{\rm merg}$, is given by $t_{\rm merg} = t_{\rm form} - t_{\rm delay}$, where $t_{\rm form}$ is the lookback time at which the particle in the Illustris TNG50 simulation has been formed.

For each of the three representative redshift snapshots from the TNG50 simulations, we divide a sample of randomly selected galaxies into four *stellar* mass bins: $8 < \log[\mathcal{M}_{\rm gal,1}/\mathrm{M}_{\odot}] < 8.75$ (referred to M1 in the figures label), $8.75 < \log[\mathcal{M}_{\rm gal,2}/\mathrm{M}_{\odot}] < 9.5$ (referred to as M2), $9.5 < \log[\mathcal{M}_{\rm gal,3}/\mathrm{M}_{\odot}] < 10.25$ (M3), and $10.25 < \log[\mathcal{M}_{\rm gal,4}/\mathrm{M}_{\odot}] < 11$ (M4). This subdivision allows us to investigate whether there is any mass dependence in the statistical properties of the BNS mergers, and, if so, whether this may affect the BNS observability in EM emission. The relative fraction of BNS merger events in each mass galaxy bin is displayed in Fig. 1 for the sample of galaxies at each redshift snapshot of our study. In each considered redshift bin, the relative fraction of BNS mergers scales with the mass of the host galaxy: The most massive galaxies tend to host more BNS mergers with respect to low mass galaxies. As already discussed in previous work (Mapelli et al. 2018; Artale et al. 2019, 2020a), the formation rate of BNSs is mainly sensitive to the star-formation rate of the host galaxy and barely affected by metallicity. Moreover, the delay time of a coeval BNS population scales as $\sim t^{-1}$ (Dominik et al. 2012; Mapelli et al. 2018, 2019). Hence, the most massive galaxies in our sample, which, at high redshift, are also associated with the highest star-formation rate, host the largest number of mergers (Artale et al. 2020a).

At low redshift ($z = 0.01$), the star-formation rate of the most massive galaxies is significantly quenched (e.g. Moffett et al. 2016). Hence, the relative fraction of BNS mergers in low-mass galaxies becomes more important at low redshift. However the amount of mass locked in the most massive galaxies at low redshift is so large (Moffett et al. 2016) that massive galaxies still dominate the merger rate per galaxy (e.g. fig. 5 of Artale et al. 2020a).

Fig. 2 shows the velocity distribution of the centre of mass of the binaries ($v_{\rm kick}$) at redshift $z = 0.01$. To make this figure, we considered the centre-of-mass velocity of each binary system after the second supernova explosion, as described in Hurley et al. (2002). The

---

[1] We note however that this is an assumption which has been debated (Beniamini & Piran 2016).

Downloaded from https://academic.oup.com/mnras/article/512/2/2654/6547794 by libraryerms@stonybrook.edu user on 05 April 2022

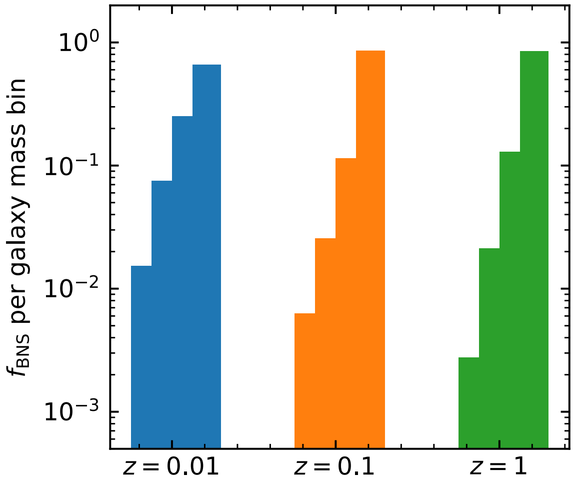

Figure 1. The fraction of BNS merger events in galaxies grouped in four mass bins (galaxy *stellar* mass). From left to right at each of the three redshift snapshots: $8 < \log[\mathcal{M}_{\rm gal,1}/{\rm M}_\odot] < 8.75, 8.75 < \log[\mathcal{M}_{\rm gal,2}/{\rm M}_\odot] < 9.5$, $9.5 < \log[\mathcal{M}_{\rm gal,3}/{\rm M}_\odot] < 10.25$, and $10.25 < \log[\mathcal{M}_{\rm gal,4}/{\rm M}_\odot] < 11$. The relative fractions are directly proportional to the mass bin, reflecting the fact that BNS mergers are produced without biases with respect to the galaxy mass, per unit mass. Note that the fractions in the various mass bins are normalized to one for each redshift snapshot; hence the relative fractions should only be compared within the same snapshot.

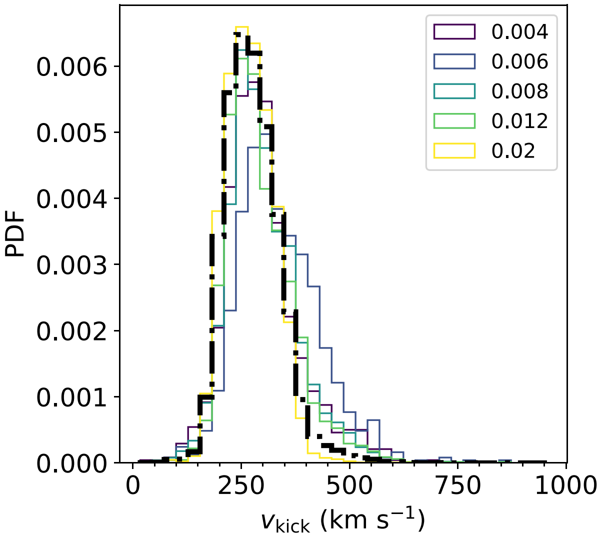

Figure 2. Probability distribution function of the binary kick velocities in the centre of mass. Black dash–dotted thick line: Kick velocities at $z = 0.01$ from the TNG50 simulation. Solid thin lines from yellow to blue: Kick velocities at $z = 0.01$ divided by the metallicity of the progenitor binary star ($Z = 0.02$, 0.006, 0.008, 0.012, and 0.02).

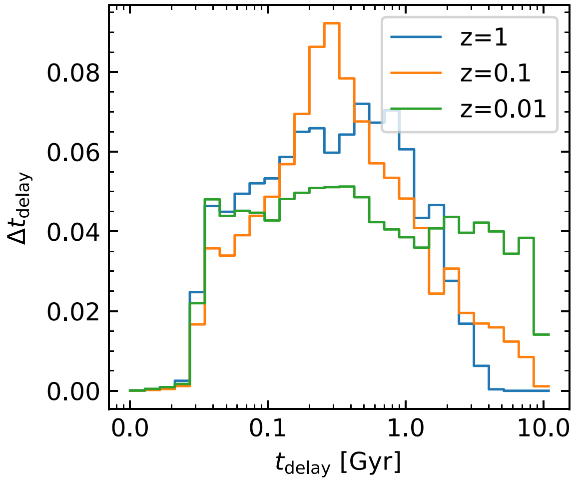

Figure 3. Distribution of the binary time delays at the three redshift snapshots of our study. These represent the times elapsed between BNS formation and BNS merger due to GW emission.

centre-of-mass velocity $v_{\rm kick}$ is very sensitive to the natal kick model we adopted in our simulations (Giacobbo & Mapelli 2020). Systemic velocities at $z = 0.01$ peak at ∼250 km s^{-1} and are mainly the fingerprint of BNSs produced by progenitors with solar and slightly subsolar metallicity (see Giacobbo & Mapelli 2020 for more details).

Fig. 3 shows the time delay distributions at the three snapshots. It is evident that the time delay is generally longer for binaries merging at lower redshifts. The delay time of a coeval population of BNSs is approximately dN/d$t \propto t^{-1}$. However what is observed at low redshift is not a single coeval population of BNSs, but rather a piling up of different populations with different ages. Most of the BNSs merging at $z \sim 0.01$ come from the tail of the t^{-1} distribution for large t and are the result of multiple episodes of star formation across the cosmic time (see fig. 4 of Mapelli et al. 2018 and Beniamini & Piran 2019 for a discussion within the context of the Galactic BNSs). On the other hand, most of the BNSs merging at $z \sim 1$ (cosmic time closer to the peak of the star-formation rate) formed in the most recent burst of star formation and come from the low t end of the t^{-1} distribution.

The velocity and time delay distributions are used to compute the distribution of the BNS merger sites, with their birth sites computed as described below. For each binary characterized by a centre-of-mass velocity $v_{\rm kick}$ and a merger time $t_{\rm delay}$, its merger location is computed by numerically integrating its orbit in the potential (stars + gas + dark matter) of the corresponding host galaxy. The direction of the kick velocity is assumed to be randomly distributed with respect to its position within the galaxy; this velocity is added to the local rotational velocity of the binary within the corresponding galactic potential assuming a random orientation for the orbit. Each orbit is integrated for a time corresponding to the delay time between the formation of the binary and its merger. We note that this procedure implicitly assumes that the galaxy potential does not evolve during the traveltime of the BNS between formation and merger. Therefore, we do not account for the changing potential that would occur if the host galaxy were to merge with another galaxy during the BNS traveltime. Various studies show that the number of galaxy mergers as a function of the cosmic time depends on both galaxy mass and redshift. Massive galaxies are more likely to be affected by major mergers during their formation assembly at high redshifts, decreasing their probability at lower redshifts (see e.g. Genel et al. 2010; Rodriguez-Gomez et al. 2015). In particular, those numerical studies with the Illustris simulation find that the rate of a major merger (i.e. between two massive galaxies with mass ratio <1/4) is <0.02 Gyr^{-1} at redshifts $z < 1$.

Fig. 4 shows the radial distribution of BNS birth sites (dashed lines) and merger sites (solid lines) for the galaxies in the four mass bins described above, and for the three redshift snapshots in our study. The distribution of the merger sites depends on the distribution of birth sites, the velocity distribution of the binaries, their traveltime

Downloaded from https://academic.oup.com/mnras/article/512/2/2654/6547794 by libraryerms@stonybrook.edu user on 05 April 2022

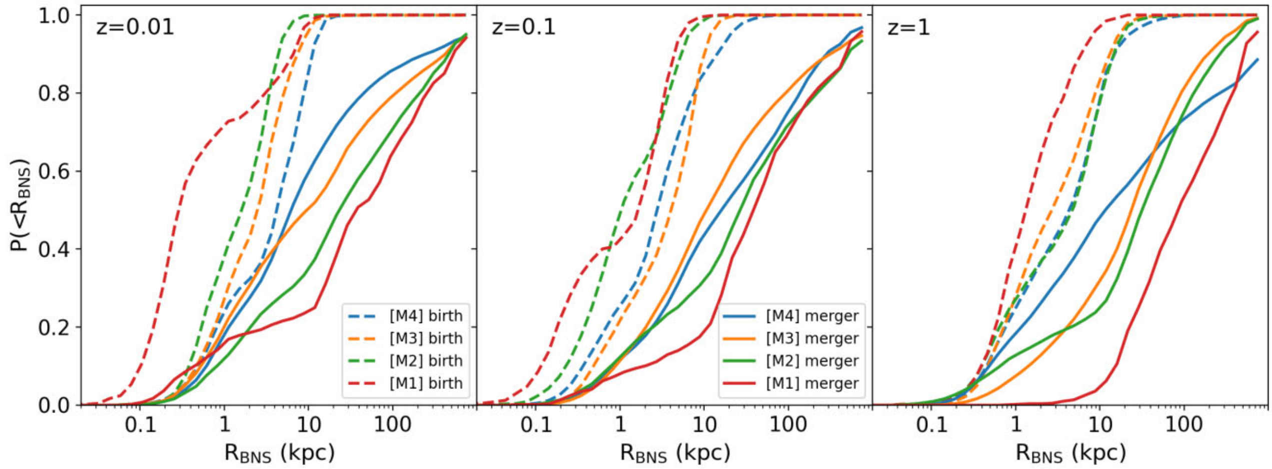

Figure 4. Radial distributions of BNS birth sites (dashed lines) and merger sites (solid lines) within their host galaxies. From left to right, the panels display the distributions at three representative redshifts from the Illustris TNG50 simulation. For each redshift, the distributions are displayed for galaxies in four *stellar* mass bins: [M1]: $8 < \log[\mathcal{M}_{\rm gal,1}/{\rm M}_\odot] < 8.75$, [M2]: $8.75 < \log[\mathcal{M}_{\rm gal,2}/{\rm M}_\odot] < 9.5$, [M3]: $9.5 < \log[\mathcal{M}_{\rm gal,3}/{\rm M}_\odot] < 10.25$, and [M4]: $10.25 < \log[\mathcal{M}_{\rm gal,4}/{\rm M}_\odot] < 11$.

up to merger (time delay), and the potential of the galaxies in which they are hosted. For a given merger location, kick velocity, and time delay, the BNSs will travel more in the smaller galaxies, due to their smaller gravitational potentials. This trend is evident in Fig. 4: For example, at all redshift snapshots, about 40 per cent of BNSs from the smaller galaxy group (M1 in the figure) is found at distances $\gtrsim$50 kpc. On the other hand, a smaller fraction reaches larger radial distances in the most massive galaxy groups. These results are in broad agreement with those of Belczynski et al. (2006). We should note that these radial distributions (and thus offset distributions) are not meant to be for direct comparison for observations of SGRBs. This is because merging BNSs can only be localized if their emission as SGRBs can be detected. However, detections are biased towards the brightest events, which are on average the ones in the innermost parts of the galaxies (see also discussion in Mandhai et al. 2021 on this point).

The distributions of the ISM densities corresponding to the merger sites distributions of Fig. 4 are displayed in Fig. 5. Each value of the distribution is essentially determined by the mass of the galaxy (less massive galaxies have on average lower ISM densities), and by the location of the BNS merger within that galaxy. Both effects contribute to an ISM density distribution which is considerably biased towards low values in the small galaxy sample, compared to the larger galaxies. As discussed in the following, the density distributions hence bias the observability of afterglow emission from BNS mergers towards larger galaxies.

2.3 EM radiation from BNS mergers

The association between GW170817 and GRB170817A has confirmed that BNS mergers yield transients with properties consistent with those of the cosmological GRBs (Lazzati et al. 2018; Mooley et al. 2018; Beniamini et al. 2019; Salafia et al. 2019). Therefore, we model the EM counterparts to the BNS mergers following the theory developed for SGRBs, and refined for the modelling of GRB170817A.

More specifically, we consider as input data a ‘structured’ jet that is a jet whose angular properties (energy distribution and Lorentz factor) have been molded by the interaction with the ejecta of a BNS merger. The jet simulations, which were performed by Lazzati et al. (2017) with the code FLASH (Fryxell et al. 2000), start with a top-hat jet of angular size 16 deg, as typically inferred for SGRBs (Fong et al. 2015), energy $L_{\rm j} = 10^{50}$ erg s^{-1}, engine duration 1 s, and Lorentz factor $\Gamma_0 = 300$, and evolve the jet within an ejecta described by a density profile $n = n_0(r/r_0)^{-2}e^{-r/r_0}$, with $r_0 = 10^{18}$ cm and $n_0 = 10^6$ cm^{-3}, made to reproduce results from realistic, general relativistic magnetohydrodynamic (GRMHD) simulations (e.g. Kawamura et al. 2016; Ciolfi et al. 2017; Radice 2017; Kiuchi et al. 2018; Foucart et al. 2019; Most, Papenfort & Rezzolla 2019; Ruiz, Tsokaros & Shapiro 2020; Camelio et al. 2021; Murguia-Berthier et al. 2021).

The prompt radiation is computed assuming that the outflow dissipates its internal energy at some radius $R_{\rm rad}$ from the engine, and the observed bolometric flux is calculated by adding the contributions of the local emission from the whole emitting surface, boosted to the fourth power of the Doppler factor $[1-\beta\cos\theta]^{-1}$, where β is the speed of the jet divided by the speed of light, and θ is the angle that the local photon makes with the normal to the emitting surface. The spectrum is assumed to be a Band one (Band et al. 1993), that is a broken power law with photon spectral indices of $\alpha_{\rm ph} = -1$ below a peak of 500 keV in the comoving frame, and $\beta_{\rm ph} = -2.5$ above it. The results of the light-curve computation are displayed in Fig. 6, which specifically shows the peak luminosity in the *Fermi/GBM* (Gamma-ray Burst Monitor) observation band. At a viewing angle of about 25–30 deg, the luminosity matches that observed in GRB170817A.

After the structured jet has released the prompt emission, it propagates into the external medium where it generates an external shock and eventually dissipates its energy. In the process, particles accelerated by the shock emit synchrotron radiation thanks to the magnetic fields generated downstream of the shock. This radiation, which spans the wide EM range from the X-rays to the radio, is the so-called afterglow. We compute afterglow light curves and spectra using standard techniques (Sari, Piran & Narayan 1998; Panaitescu & Kumar 2000; Granot et al. 2002; Rossi et al. 2004; Beniamini, Granot & Gill 2020), involving the integration of the local emission over the equal arrival times, for an observer located at any line of sight with respect to the jet axis. The afterglow radiation depends on the microphysical shock parameters that describe the particle distribution and magnetic field intensity downstream the shock. These are parametrized via the fraction $\epsilon_{\rm e}$ of energy which

Downloaded from https://academic.oup.com/mnras/article/512/2/2654/6547794 by libraryerms@stonybrook.edu user on 05 April 2022

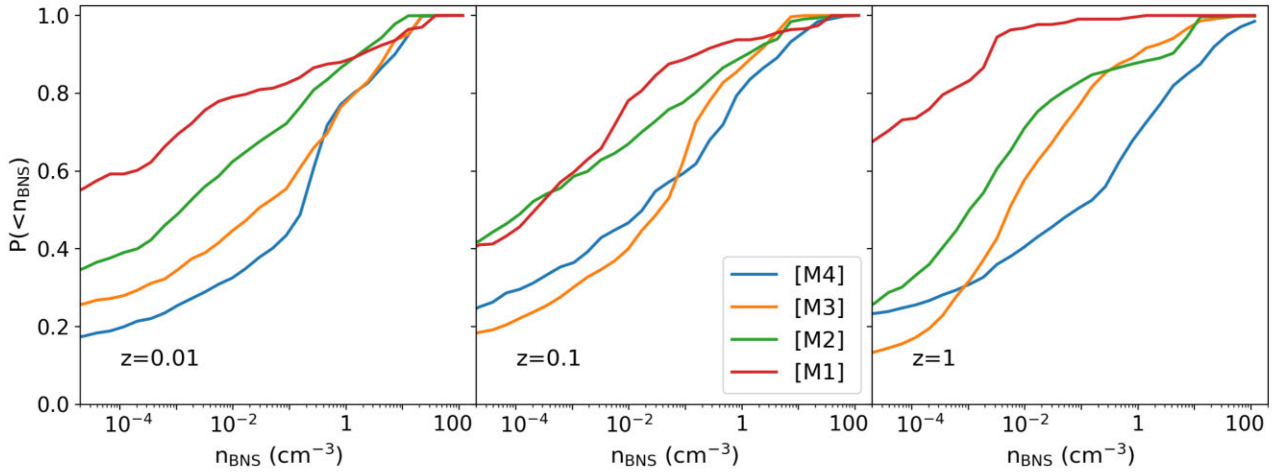

Figure 5. Distribution of interstellar medium (ISM) densities at the BNS merger site locations. From left to right, the panels display the distributions at three representative redshifts from the Illustris TNG50 simulation. For each redshift, the distributions are displayed for galaxies in four *stellar* mass bins: [M1]: $8 < \log[\mathcal{M}_{\rm gal,1}/{\rm M}_\odot] < 8.75$, [M2]: $8.75 < \log[\mathcal{M}_{\rm gal,2}/{\rm M}_\odot] < 9.5$, [M3]: $9.5 < \log[\mathcal{M}_{\rm gal,3}/{\rm M}_\odot] < 10.25$, and [M4]: $10.25 < \log[\mathcal{M}_{\rm gal,4}/{\rm M}_\odot] < 11$.

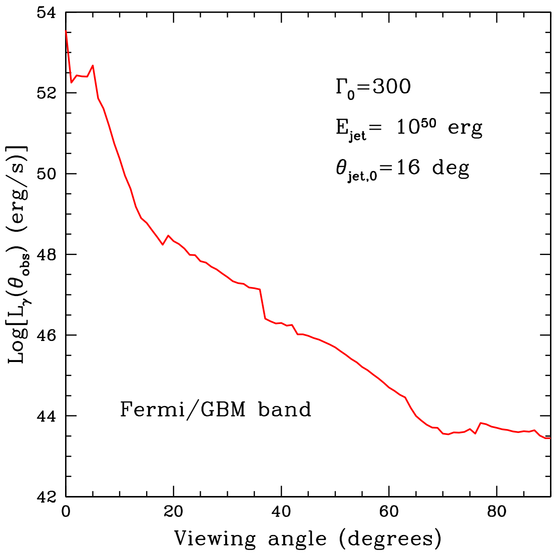

Figure 6. Isotropic peak luminosity in the *Fermi/GBM* band as a function of the viewing angle with respect to the jet axis. The initial jet parameters are those typical of a SGRB, and the luminosity at $\theta_{\rm obs} \sim 25$–30 deg matches that of GRB170817A.

goes to the electrons, and the fraction $\epsilon_{\rm B}$ of energy which goes into the magnetic field. Here, we adopt the values of these parameters which provided the best fit to the broad-band light curves of GRB170817A: $\epsilon_{\rm e} = 0.03$ and $\epsilon_{\rm B} = 0.003$, and the index of the electron distribution $p = 2.13$. With these fixed, we ran a grid of light curves for a range of number densities of the ISM between 10^{-6} cm^{-3} and 100 cm^2.

Fig. 7 shows, for two representative viewing angles $\theta_{\rm view} = 2$ deg (top panels) and $\theta_{\rm view} = 45$ deg (bottom panels) with respect to the jet axis, the afterglow light curves in three representative bands (X-rays, optical, and radio) for a range of number densities in the interval $n = [10^{-3}$–$10]$ cm^{-3}, which encompasses a good fraction of the density values expected at the BNS merger sites (cfr. Fig. 5). A visual comparison between upper and lower panels (note the same scale on the *y*-axis) immediately highlights the strong dependence of the luminosity on the viewing angle with respect to the line of sight to the observer. Hence, GW-detected BNS mergers, which are more likely to be seen at larger viewing angles with respect to the cosmological SGRBs, are expected to have on average significantly dimmer luminosities than these bursts, which can only be detected when close to on-axis.

An important feature to notice of the off-axis afterglow light curves is that their peak brightness occurs much later than for the on-axis GRBs. This is because the maximum luminosity is achieved when the Doppler factor of the emitting jet becomes on the order of $\Gamma \sim 1/\theta_{\rm view}$, and hence radiation from the more energetic central regions of the jet can reach the observer. The specific time at which this happens depends on the medium density. At higher densities, the blast wave decelerates more quickly, and emission from the central jet regions enter the line of sight at earlier times. At 45° angle, all frequencies shown are above the self-absorption frequency, and therefore the peak luminosity is larger for larger densities in all the bands, reflecting the larger fraction of emitting electrons for higher densities (see e.g. Sari et al. 1998). On the other hand, the radio band is below the self-absorption frequency for the on-axis light curves, causing the radio emission in denser media to be dimmer due to the larger opacity of the blast wave.

Another feature of the light curves which is worth noticing (and which will play a role in the interpretation of the statistical results for the EM emission), is the fact that, while at small viewing angles (upper panels) the peak specific flux of the radio emission is comparable to that in the optical, and only moderately larger than the peak flux in X-rays, at large viewing angles (bottom panels), the radio brightness is significantly larger than the optical, and even more so than the X-ray one. This is because the physical reason for the peak of the light curves in different bands is different for on- and off-axis observers. For on-axis observers the peak is due to the fact that the spectrum moves towards lower frequencies as the fireball decelerates, maintaining a constant peak specific flux (Sari et al. 1998). Higher frequencies peak earlier in time but, as long as there is no self-absorption, all bands peak with the same specific flux. For off-axis viewers, instead, the peak is due to the entering of the core emission within the line of sight. While the wings contribute to the observed emission, the core dominates at all bands after it becomes visible. In this case the peak happens almost simultaneously in all bands, since it is a geometric effect. In most relevant cases, since the emission peak is seen at large angles form the core and at late times, the peak frequency is at low frequencies and lower frequencies

Downloaded from https://academic.oup.com/mnras/article/512/2/2654/6547794 by libraryerms@stonybrook.edu user on 05 April 2022

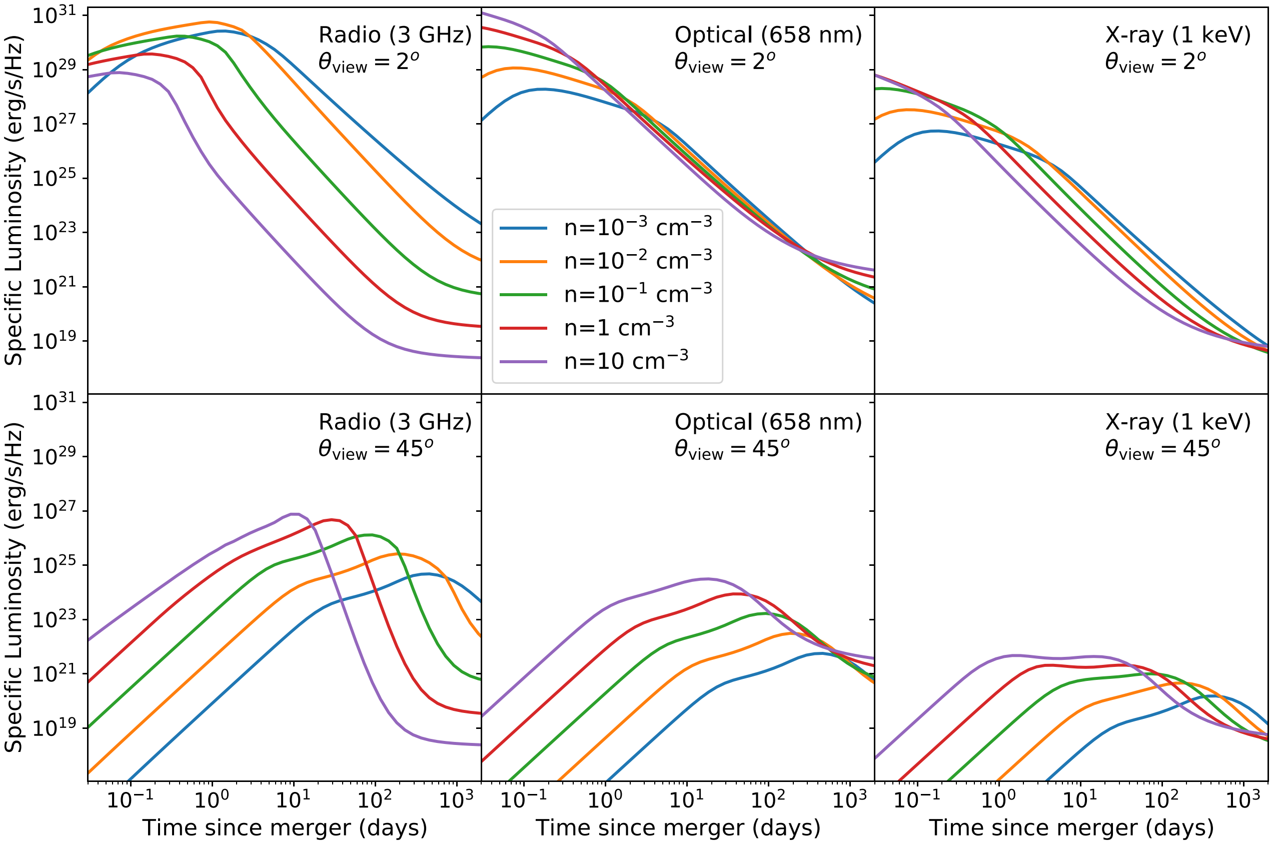

Figure 7. ISM density dependence of the afterglow luminosity density in three representative bands (radio, optical, and X-rays; from left to right) and for an on-axis viewing angle ($\theta_{\rm view} = 2$ deg, top panels), or for a more generic and likely viewing angle, $\theta_{\rm view} = 45$ deg (bottom panels) with respect to the jet axis. Note that the scale on the y-axis is the same in all the panels, highlighting the significant drop in luminosity at larger viewing angles.

appear brighter for off-axis observers. This results in a ratio between the radio and the X-ray peak fluxes which is much larger at larger viewing angles than near the core.

The grid of light curves will be used, together with the information on the BNS sites provided by the calculations described in Sections 2.1 and 2.2, to predict the statistical properties of the BNS EM counterparts in Section 3.

3 RESULTS: MONTE CARLO SIMULATION OF THE EXPECTED EM SOURCE POPULATION

We generate the observable population, at each redshift snapshot and for each of the four galaxy mass bins, by performing Monte Carlo random realizations for each of these subpopulations. For each case we run 10^5 different random realizations. The merger sites are drawn from the probability distributions of Fig. 4, and the corresponding ambient densities from the curves of Fig. 5. The inclination angle of the jet is assumed to be isotropically distributed on the sky.

Fig. 8 shows the distributions of gamma-ray fluxes (prompt emission) from BNS mergers in host galaxies at our three representative redshifts $z = 0.01$, 0.1, and 1 (corresponding to luminosity distances of about 45 Mpc, 480 Mpc, and 7 Gpc, respectively). Since the prompt emission is independent of the ambient medium of the host galaxies, the BNS population has not been subdivided by groups in galaxy mass. The relative number of prompt (gamma-ray) events for each galaxy mass bin is simply proportional to the relative number of BNS mergers in that mass range (cfr. Fig. 1). For an immediate gauging of the fraction of detectable events by current gamma-ray detectors, the vertical line indicates the flux value 10^{-8} erg cm^{-2} s^{-1}, corresponding to the detection threshold of the *Swift BAT* (Burst Alert Telescope) detector for a typical GRB spectrum.[2] In the case of the *Fermi BAT* detector, the sensitivity is provided in photon counts,[3] and the conversion to fluence requires a spectral assumption. However, noting that the weakest detected burst in the Fermi catalogue (Bhat et al. 2016) has a flux 2×10^{-8} erg cm^{-2} s^{-1}, we can assume that the threshold fluxes of the two instruments are roughly comparable. The figure shows that the fraction of detectable events is quite small, $\sim$2 per cent, at the highest simulated redshift of $z = 1$, and it remains still small, $\sim$10 per cent at the $z = 0.1$ snapshot. The small probability of a prompt gamma-ray detection at these higher redshifts is a result of the fact that since the direction of the jet axis is assumed to be uncorrelated with the viewing angle, a large majority of events are being caught at large viewing angles, where the luminosity is considerably dimmer (cfr. Fig. 6).

The smallest redshift of $z = 0.01$, corresponding to a luminosity distance of about 45 Mpc, is within the current horizon of LIGO and Virgo to BNS mergers (Abbott et al. 2016), and it is comparable to the distance of GW170817 (Abbott et al. 2017a). At this distance, about 40 per cent of the gamma-ray counterparts to BNS mergers are expected to be detected by current satellites. This probability is

---

[2] https://swift.gsfc.nasa.gov/about_swift/bat_desc.html

[3] https://gammaray.msfc.nasa.gov/gbm/instrument/

Downloaded from https://academic.oup.com/mnras/article/512/2/2654/6547794 by libraryerms@stonybrook.edu user on 05 April 2022

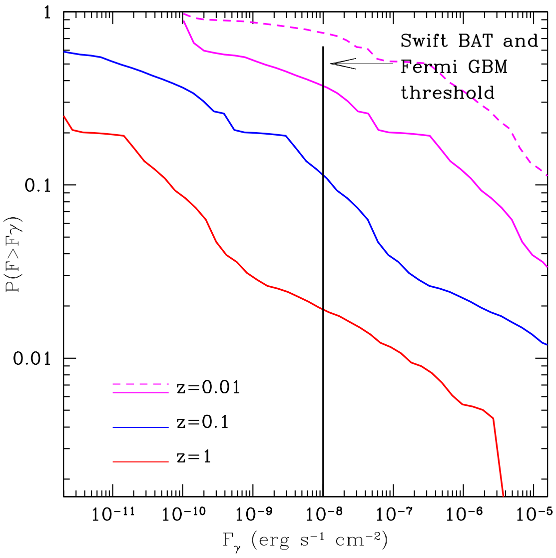

Figure 8. The fraction of BNS merger events, with jet properties similar to those of GRB170817A, which have peak flux in gamma-rays larger than F_γ, as a function of F_γ and for four different distances. The smallest distance of $z = 0.01 \sim 45$ Mpc is within the current horizon of LIGO–Virgo for BNS mergers. The orientation of the jet with respect to the observer is assumed to be random on the sky except for $z = 0.01$, where both the random orientation (solid line) and the GW-detected case (dashed line) have been simulated. As expected, at cosmological distances the detectable fraction of gamma-ray events with current detectors is rather small, since the luminosity drops rapidly with angle (cfr. Fig. 6) and hence only jets observed at small enough viewing angles are luminous enough to allow detection. Note that the displayed probabilities do not account for the field of view of the instruments (9.5 sr for *Fermi* and 1.5 sr for *Swift*).

enhanced if we account for the fact that for BNS mergers whose first trigger is in GWs, the viewing angle may be correlated with the jet axis. More specifically, if the jet axis is in the direction of the orbital angular momentum of the binary, then the distribution of viewing angles will be determined by the detection probability of GW detectors. We hence consider also this situation, which is the relevant one for events within the LIGO–Virgo horizon. The detection probability as a function of the angle i between observer and rotation axis of the binary can be written as (Schutz 2011)

$$P(i) = 0.076076\ (1 + 6\cos^2 i + \cos^4 i)^{3/2}\ \sin i. \tag{3}$$

For the lowest redshift of $z = 0.01$ we ran a Monte Carlo simulation with the assumption that the viewing angle with respect to the jet, that is $\theta_{\rm view}$ is equal to i. The results are shown with the dashed line in Fig. 8. The detection probability with the *Fermi* and *Swift* satellites rises to about 75 per cent. One point to note is that, to read off all the curves in Fig. 8 as actual observing probabilities without any prior on the sky localization, they should be corrected for the field of view of the observing instruments. This is 9.5 sr for *Fermi* (giving a correction factor of ∼0.75, and 1.5 sr for *Swift* (giving a correction factor of ∼0.1).

For the longer wavelength (afterglow) radiation, we perform different sets of calculations for the $z = 0.01$ snapshot than for the $z = 0.1$ and $z = 1$ snapshots. For the former, which is well within the current horizon for GW detections, we simulate the two cases discussed above for a GW-triggered event: random viewing angle if the jet direction is uncorrelated with the orbital plane of the binary, and viewing angle drawn from the probability distribution in equation (3) if the jet is pointing roughly perpendicular to the orbital plane of the merging NSs. On the other hand, for the higher redshift snapshots which are beyond the GW current horizon to BNS mergers, we simulate the current astrophysical scenario of the 'standard' cosmological SGRBs, which are first triggered in gamma-rays, and then followed at longer wavelengths. Hence for these we will restrict the distribution of viewing angles to those for which the prompt emission is above the detection threshold of *Swift* and *Fermi*.

Figs 9 and 10 show the fraction of afterglows from BNS mergers with flux larger than a certain value (displayed on the y-axis), as a function of time from the merger, in three different observation bands: radio, optical, and X-rays; from left to right. For each flux, the probabilities are separately displayed for BNS merger events in the four mass bins of our study. While Fig. 9 assumes a random distribution for the viewing angle with respect to the emitting jet, Fig. 10 has been computed with the viewing angles drawn from the probability distribution in equation (3). The contour lines in both figures represent the fraction of simulated events with flux above the corresponding values on the y-axis, at the observing times (from the time of merger) indicated in the x-axis. A common feature among all panels is that bright events only happen at earlier times and with small probability, with the dimmest, late-peaking events being more probable. This is due to the fact that both increasing the viewing angle and decreasing the interstellar density result in less bright events that peak at late times (weeks to months). The prevalence of intermediate densities (Fig. 5) and the geometry that favours large viewing angles results in rare, early-peaking, bright events and more common, late-peaking dim events. Events peaking at more than a few months are instead extremely rare because the viewing angle cannot exceed 90° and binaries merging in extremely low densities are rarer (Fig. 5).

A visual comparison between Figs 9 and 10 shows that the latter has a larger fraction of brighter events, and that the time from the merger at which the events reach their maximum brightness is typically smaller. This results from the fact that the events in Fig. 10 are selected with a bias towards smaller viewing angles with respect to the completely random selection of the events in Fig. 9. Smaller viewing angles imply both brighter emission as well as earlier peak emission.

The figures also indicate, with a horizontal line, representative threshold detections of current instruments, that is *Chandra* and *Swift* in X-rays, *Hubble Space Telescope (HST)* and Robotic follow-up for the optical, and a 1 h integration time on the Very Large Array (VLA) for the radio. These instruments were among the ones which detected the afterglow emission of GRB170817A. The results of Fig. 10 imply that an event like GRB170817A, which was initially triggered in GWs and which had a viewing angle inferred from EM emission consistent with that from GWs, had a probability ∼0.5 of being observed in all afterglow wavelength bands (recall the redshift of $z = 0.01$ corresponds to a distance of 45 Mpc, close to that of GW/GRB170817A).

Next we examine the dependence on the galaxy mass, studied by means of the four rows in Figs 9 and 10. In both cases, there is a clear bias against detection of events from smaller galaxies. The exact value varies depending on the band, and is slightly different between the two choices of viewing angles. A quantitative comparison between the peak emission from events in the least massive galaxy group (M1) and the most massive one (M4) shows that, for example, in the radio band, there is an enhanced probability by a factor of ∼2.5: 1 of detecting an event from a massive galaxy than one from a smaller one (assuming the intrinsic number of events being the same). Therefore, in addition to being disfavoured by event number (cfr. Fig. 1), BNS mergers in small galaxies suffer

Downloaded from https://academic.oup.com/mnras/article/512/2/2654/6547794 by libraryerms@stonybrook.edu user on 05 April 2022

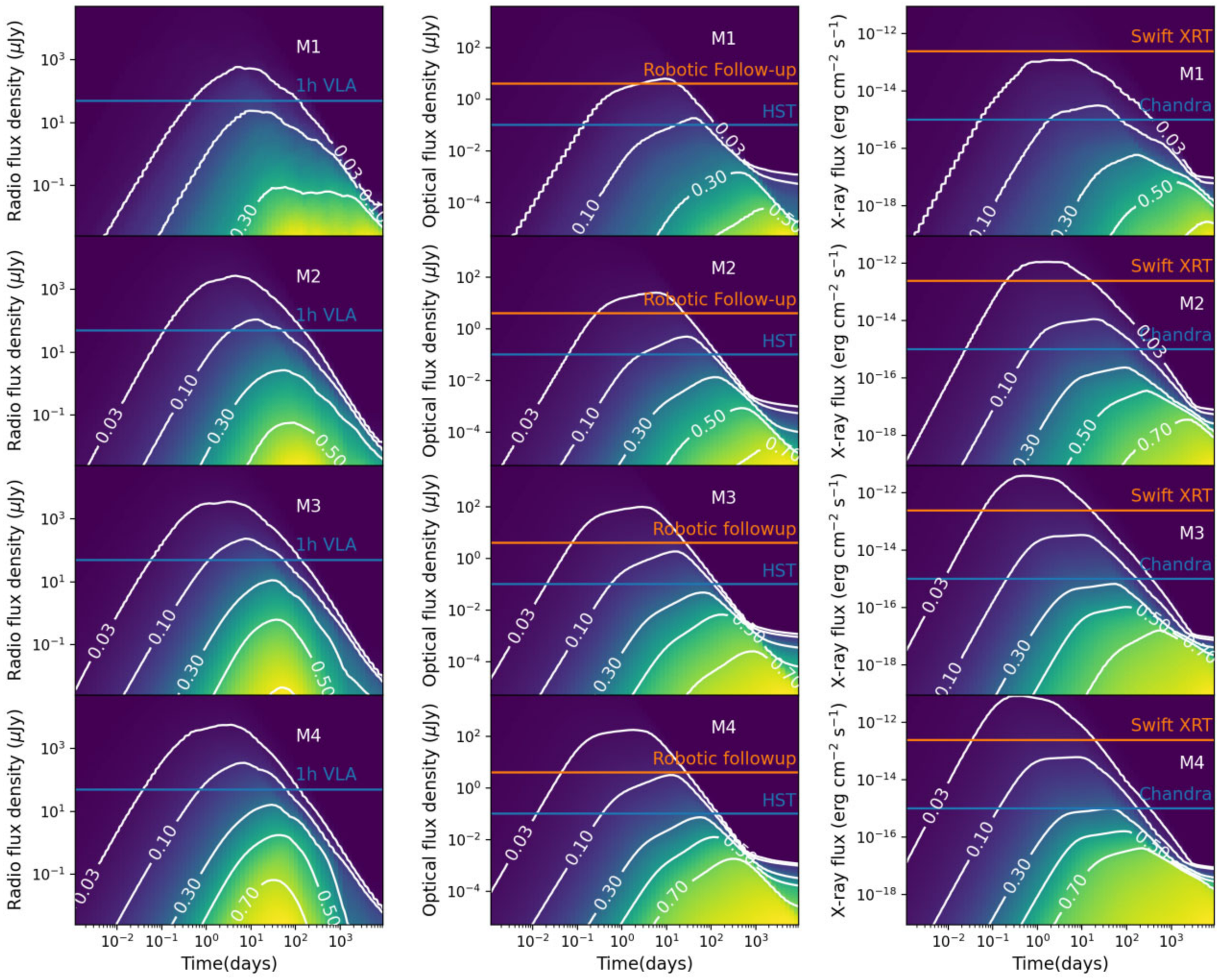

Figure 9. Probability of detecting an EM counterpart in three wavelength bands (radio, optical, and X-rays; from left to right) as a function of time from the merger event, for BNS mergers in galaxies at the redshift snapshot $z = 0.01$. From top to bottom, the various panels refer to the four galaxy mass bins of our study. The numbers in the contour lines represent the fraction of BNS mergers with flux larger than the corresponding value (on the y-axis) at the corresponding time to the x-axis. Here, the viewing angle with respect to the jet axis is drawn from a random distribution.

by a selection bias, which makes their detectable fraction suppressed compared to the intrinsic value. This results from the combinations of two factors: (i) in small galaxies the ISM density is generally lower than in larger ones; and (ii) in smaller galaxies, BNSs travel to further distances given the smaller potential (cfr. Fig. 4), hence further contributing to a lower density of the ISM at their merger sites (cfr. Fig. 5).

For the higher redshifts snapshots $z = 0.1$ and $z = 1$, which are beyond the current LIGO–Virgo horizon we simulate the statistical properties of the EM counterparts from BNS mergers as for the standard cosmological SGRBs. More specifically, we consider a random distribution on the sky of the viewing angle $\theta_{\rm view}$ with respect to the observer line of sight. We then compute the gamma-ray flux in the *Swift/XRT* (X-ray Telescope) and *Fermi/GBM* bands. As observed above, the threshold sensitivities are roughly comparable for these two instruments. If the flux is above the detection limit, then we compute its afterglow based on the merger location of the BNS within its corresponding host galaxies. Given the anticorrelation between flux and viewing angle (cfr. Fig. 6), this procedure is practically equivalent to selecting the maximum viewing angle, $\theta_{\rm view,\,\gamma}$, which can allow detection at the given redshift. We find $\theta_{\rm view,\,\gamma} \sim 29.4$ deg for merger events at $z = 0.1$, and $\theta_{\rm view,\,\gamma} \sim 11.5$ deg for those at the redshift $z = 1$.

The detection probabilities for the afterglows of the SGRBs triggered in gamma-rays are given in Figs 11 and 12 for the two redshifts $z = 0.1$ and $z = 1$, respectively. The general trends with galaxy mass are similar to those found at $z = 0.01$, and that is that low-mass galaxies are selectively disfavoured for afterglow detection. Since this is the key to localize the burst and hence measure its redshift via host galaxy identification, we conclude that the population of SGRBs does not represent an unbiased distribution with respect to the underlying one with respect to the galaxy host. This needs to be kept in mind when comparing theoretical models of SGRBs from BNSs with the statistical properties of their host galaxies.

If the afterglow properties of GRB170717 are indeed representative of the bulk of the cosmological SGRBs, then our simulations predict that at least half of the events should be detectable with current X-ray detectors and an optical telescope such as the *HST*. In the radio, an hour of integration time with the VLA yields $\lesssim 10$ per cent of detectable events.

Generally speaking, the relative observability in different bands depends on both the viewing angle and the ambient density. The latter is a more important factor for the radio band than the X-ray band at the times at which the emitting flow is in the so-called synchrotron radiative regime, i.e. a regime in which radiative losses are significant. This regime, which is satisfied at emitting frequencies

Downloaded from https://academic.oup.com/mnras/article/512/2/2654/6547794 by libraryerms@stonybrook.edu user on 05 April 2022

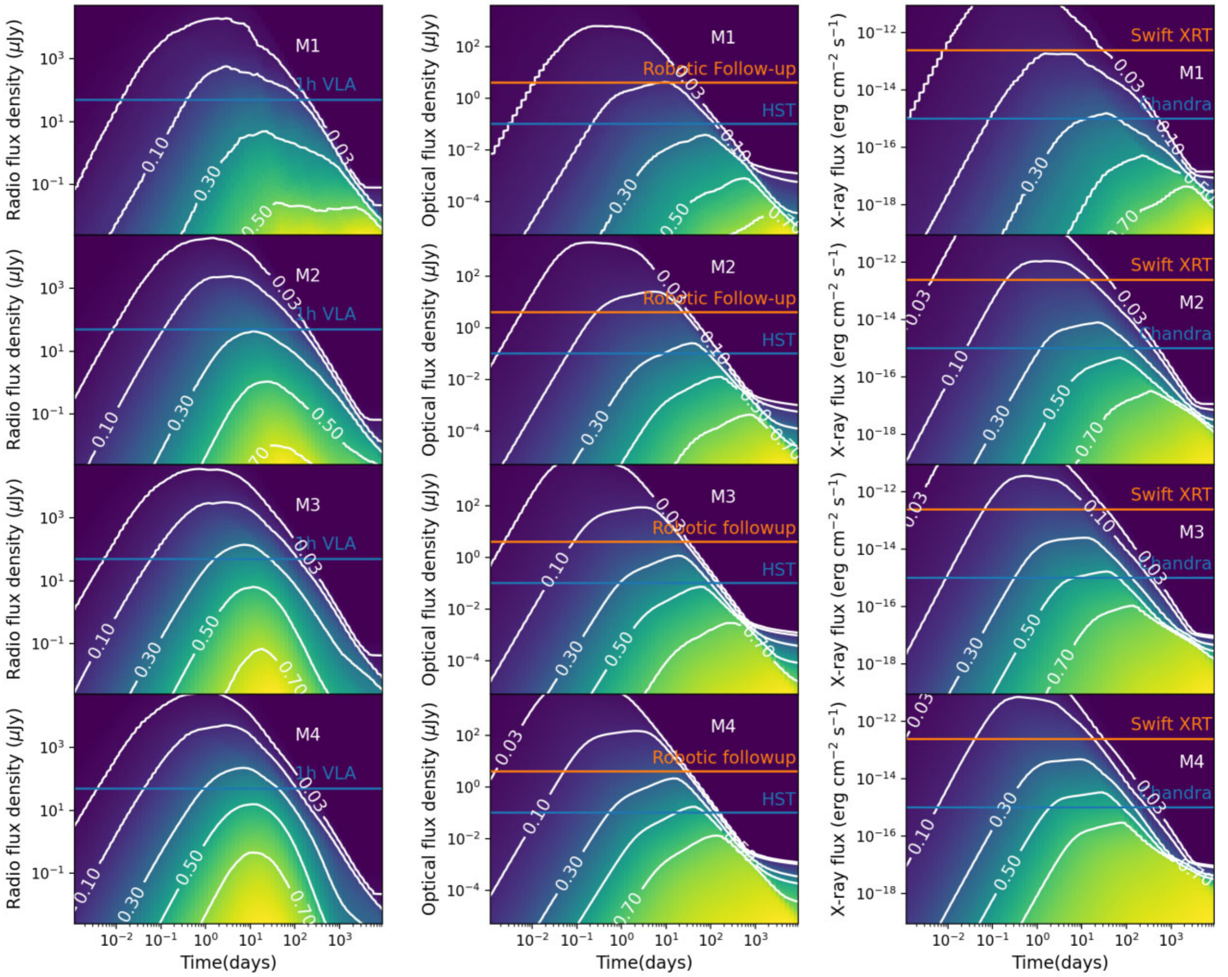

Figure 10. Same as Fig. 9 but with the jet angle assumed to coincide with the perpendicular to the orbital plane of the binary, and hence the probability distribution for the viewing angle (assuming a GW trigger) given by equation (3).

above a critical frequency value, is hence more likely satisfied for the higher energy bands than the lower one. Once in this regime, the emission becomes independent of the ambient density (Sari et al. 1998, see also discussion in Saleem et al. 2018).

A noticeable difference between the population of GW-detected afterglow counterparts, and the population of gamma-ray triggered afterglow counterparts at the higher redshift snapshots $z = 0.1$ and $z = 1$, is the fact that in the latter cases, the relative fraction of X-ray to radio (and optical) detectable counterparts is significantly higher than for the former. This is a direct consequence of the fact that gamma-ray triggered events are generally selecting out at much smaller viewing angles than GW-detected events. As shown by Fig. 7 and discussed in the corresponding text, at smaller viewing angles the X-ray/radio relative flux is much larger than it is when the event is observed from large viewing angles. For this reason, since the maximum viewing angle $\theta_{\rm view,\,\gamma}$ (to trigger bursts in gamma-rays) is smaller for the $z = 1$ events than it is for the $z = 0.1$ ones, the tendency for the X-ray flux to be brighter than the radio one is further enhanced in the higher redshift snapshot than it is in the $z = 0.1$ one.

We note that in the Monte Carlo simulations leading to Figs 10–12 we did not include the contribution from the kilonova, which was observed for GW170817 (Abbott et al. 2017c; Arcavi et al. 2017; Chornock et al. 2017; Coulter et al. 2017; Cowperthwaite et al. 2017; Drout et al. 2017; Kasen et al. 2017; Pian et al. 2017; Smartt et al. 2017; Soares-Santos et al. 2017; Tanvir et al. 2017). The maximum flux in the optical (red) was around 200 μJy at about 1 d. At the redshift of $z = 0.01$ (roughly the distance to GW170817), this luminosity is comparable to the brightest afterglows in Fig. 9 and 10. More specifically, the kilonova luminosity exceeds the maximum afterglow luminosity (in the red band used here) for viewing angles $\theta_{\rm view} \gtrsim 10$ deg for an ambient density $n_{\rm ISM} = 0.01$ cm^{-3} (higher densities correlate with larger values of $\theta_{\rm view}$ for the kilonova and afterglow luminosities to be comparable, and vice versa).

We further note that the afterglow calculations have not included absorption by line of sight material within the host galaxy. This might affect optical and X-ray detectability due to dust absorption and photoionization, respectively. Modelling this effect would require assumption on metallicity and dust to gas ratios (as well as tracking their time dependence due to the burst radiation, see Perna, Lazzati & Fiore 2003) that are uncertain and beyond the scope of this work.

In order to more directly connect with observational predictions for EM counterparts detectability, in Fig. 13 we show the fraction of events with flux larger than the flux limit in our three representative bands, using the *Chandra* limit in X-rays, the *HST* limit in the optical, and 1 h integration time for the VLA. The fractions are shown as a function of time, and represent the integration of the events over all the mass bins within the corresponding time interval of the bin. As such, they are dominated by the largest galaxies (cfr. Fig. 1). For the $z = 0.01$ snapshot, we considered the case of random inclination of the viewing angle, for homogeneity with the higher redshift snapshots

Downloaded from https://academic.oup.com/mnras/article/512/2/2654/6547794 by libraryerms@stonybrook.edu user on 05 April 2022

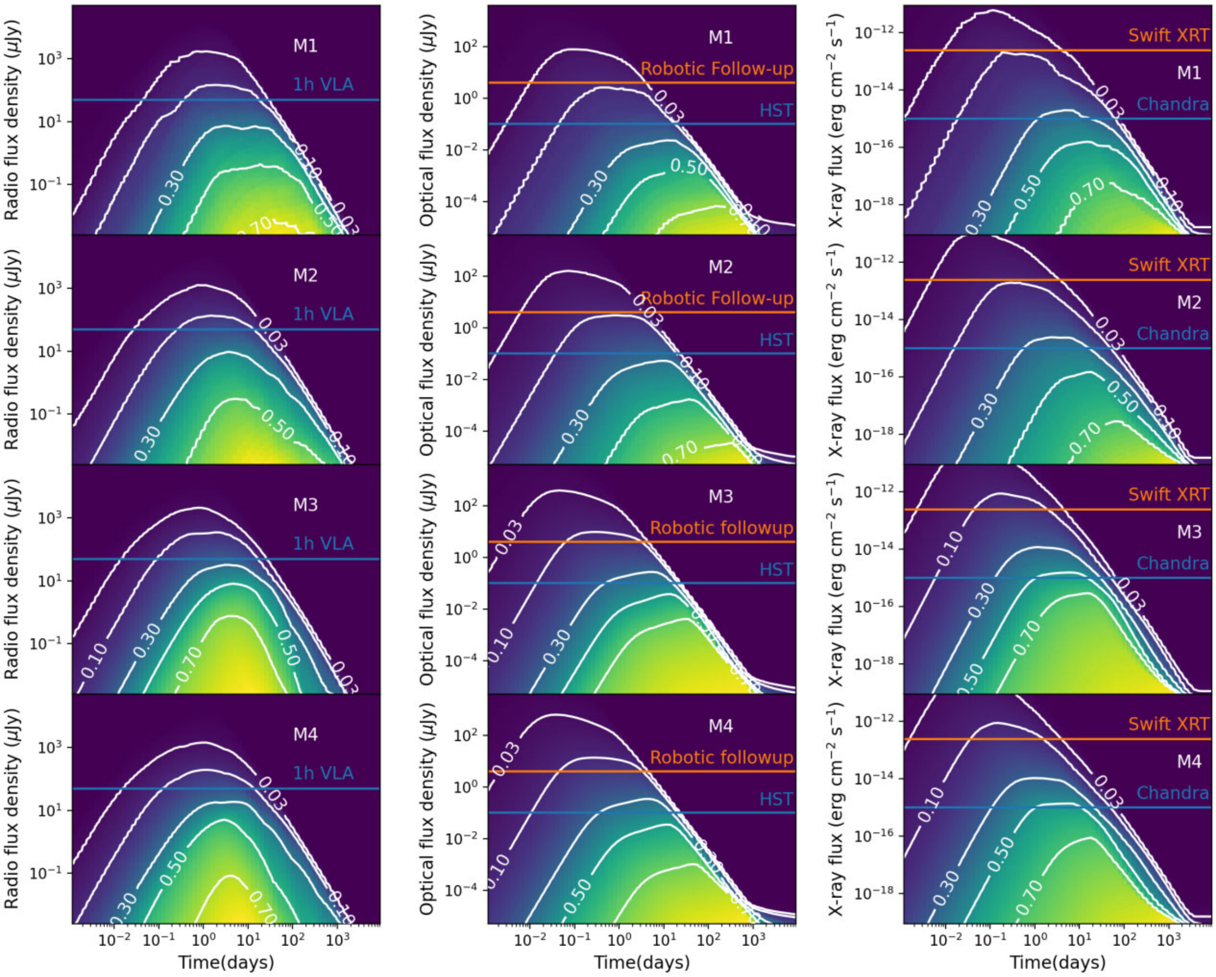

Figure 11. Same as Fig. 9 but for the sample of galaxies at the redshift snapshot $z = 0.1$, and with the condition of a viewing angle (with respect to the jet axis) randomly chosen but such that $\theta_{\rm view} \le \theta_{\rm max,\,\gamma}$, where $\theta_{\rm max,\,\gamma}$ is the maximum value for which the gamma-ray emission is large enough to trigger the *Swift/BAT* and *Fermi/GBM* detectors. At the redshift of $z = 0.1$, we find $\theta_{\rm max,\,\gamma} \sim 29.4$ deg, for the GRB170817A-like event adopted here. This situation simulates the one of the standard cosmological SGRBs; that is BNS mergers outside of the current LIGO–Virgo GW horizon, which are routinely triggered by their prompt gamma-ray emission and later searched at longer wavelengths.

displayed in the same panels. The general trend is for the higher redshift events to have a higher probability to be detected at earlier times (as already shown by a visual comparison of Figs 9, 11, and 12), but more evident here as the results for the different redshifts are displayed in the same panel. Physically, this is due to the fact that events from higher redshifts are detected for smaller viewing angles, when the emission is brighter at earlier times (cfr. Fig. 7). EM counterparts from $z \sim 1$ have a highest chance to be detected on a time-scale of a few hours, whereas events from $z \sim 0.01$ become brighter after several days to several weeks.

Before summarizing and concluding, we remind the reader that all the numbers quoted in this result section are ‘theoretical’, i.e. simply computed assuming that the source flux exceeds the flux limit of the instrument. In practice, an actual detection may require a certain signal-to-noise ratio, and hence this would reduce the fraction of what are considered detections.

4 SUMMARY AND DISCUSSION

The association of GW170817 with GRB170817A, and the recognition that the latter has properties fully consistent with those of the standard cosmological SGRBs, has opened a new line of investigation of SGRBs, and in particular their detectability in connection with GW-triggered BNS mergers. The observed variety of SGRB luminosities is consistent with being largely driven by viewing angle effects, with GRB170817A being a rather typical event among the well-studied set of cosmological SGRBs (Wu & MacFadyen 2019).

In this work we have performed a comprehensive study of the EM counterparts expected from BNS merger events, using the intrinsic source properties of GRB170817A as a template. Our population of BNSs is generated via population synthesis calculations with the code MOBSE, and seeded in a sample of galaxies from the TNG50 simulation, at three representative redshifts of $z = 0.01$, 0.1, and 1, straddling the range of GW-detected events and that of the standard cosmological SGRBs, detected in gamma-rays.

We have studied the BNS population by dividing their host galaxies from the TNG50 simulation in four mass groups at each redshift snapshot, with the goal of uncovering possible biases of the observed population with respect to the intrinsic one. Our analysis uncovered that such biases do indeed exist.

Downloaded from https://academic.oup.com/mnras/article/512/2/2654/6547794 by libraryerms@stonybrook.edu user on 05 April 2022

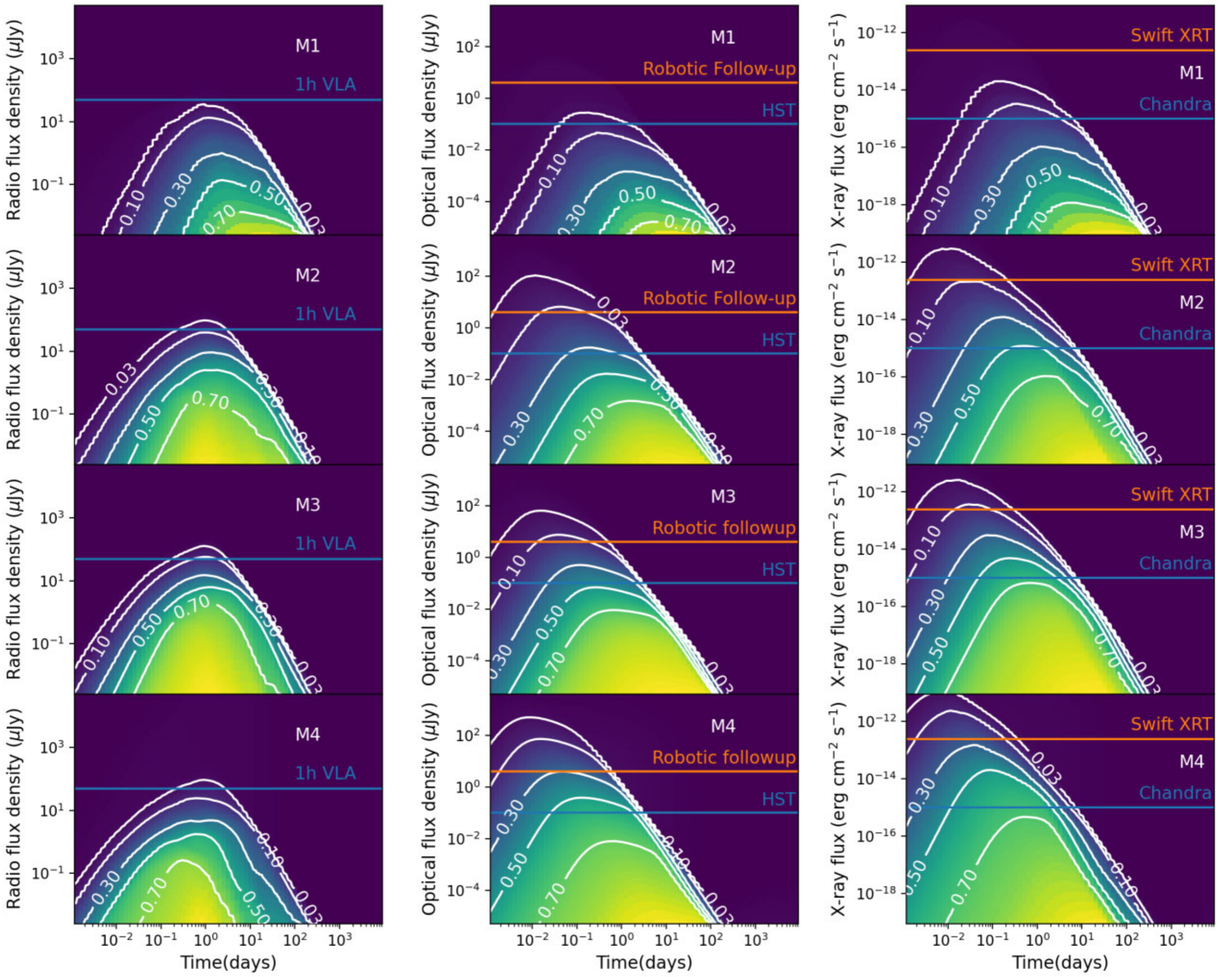

Figure 12. Same as Fig. 11 but for the sample of galaxies at the redshift snapshot $z = 1$, with the condition of a viewing angle smaller than a maximum value to allow gamma-ray trigger of the event by the *Swift/BAT* and *Fermi/GBM* detectors. At the redshift of $z = 1$, we find $\theta_{\max,\gamma} \sim 11.5$ deg.

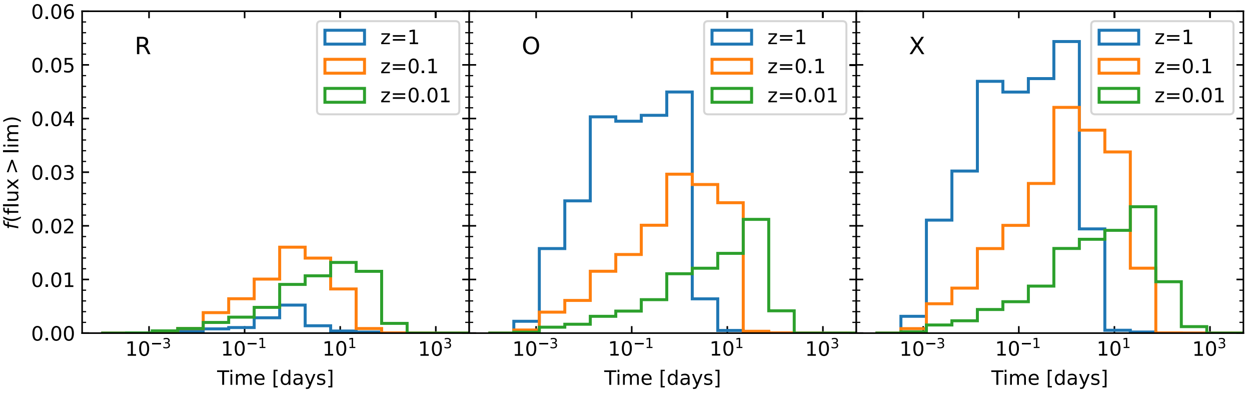

Figure 13. Fraction of events (summed over all galaxies in the sample for each redshift snapshot) with flux larger than the flux limit in the corresponding time-interval bin. The value of the flux limit has been assumed to be 1 h integration on VLA in radio, the *HST* limit for the optical, and the *Chandra* limit in X-rays. For the $z = 0.01$ case we considered the scenario of random viewing angle, for homogeneity with the higher redshift cases.

Additionally, the comparative analysis of the afterglow counterparts to GW-triggered events, versus gamma-ray triggered events (i.e. the standard cosmological GRBs) has uncovered some interesting differences among the two populations, even as the underlying source is the same.

Our main results are summarized in the following:

GRB170817A, first detected in GWs and later followed up in the EM spectrum, appears to be a rather common/typical event for the BNS merging population. Our population synthesis calculations of BNSs at the redshift snapshot $z = 0.01$ of the TNG50 simulation,

Downloaded from https://academic.oup.com/mnras/article/512/2/2654/6547794 by libraryerms@stonybrook.edu user on 05 April 2022

which, corresponding to a distance of ∼45 Mpc, is very close to that of GW170817 (40 Mpc), shows that the broad-band detection of GRB170817A had a sizeable probability.[4] In gamma-rays, the *Fermi GBM* detector would have ∼30 per cent probability to detect such an event if its EM emitting jet were uncorrelated with the orbital plane of the merging NSs (having corrected the detection probability of Fig. 8 by the field of view of 9.5 sr of this telescope), and of ∼60 per cent for the situation in which the relativistic jet is roughly aligned with the orbital angular momentum of the binary, as found to be the case for this source (and again taking into account the reduction in probability due to the limited field of view of the telescope).

Our calculations of the distribution of the merger sites of BNSs within the sample of galaxies from the TNG50 simulation has allowed us to predict the distribution of ISM densities, and thus the afterglow brightness as a function of time and wavelength. At the redshift of $z = 0.01$, about 20–30 per cent of BNS mergers are expected to have detectable afterglow radiation for randomly oriented jets, whereas the fraction is enhanced to ∼40−50 per cent for jets aligned with the orbital angular momentum of the binary (these probabilities assume prior localization from the prompt emission). Therefore, the binary NS merger event GRB170817A appears to be representative of the theoretically predicted population of BNS mergers in the local Universe.

To date, there has been only one other reported GW-detected BNS merger event, GW190425 (Abbott et al. 2020), at a distance of about 155 Mpc. Both the *Fermi/BAT* (Fletcher, Fermi-GBM Team & GBM-LIGO/Virgo Group 2019) and the *Swift/XRT* telescopes (Sakamoto et al. 2019) were located in unfavourable positions for observability, with ∼45 per cent of the GW localization area located behind the Earth. This, combined with the large distance of the event prevented a precise localization of the source, hampering follow-up from ground-based observatories. Several candidate transients were detected, but were all eventually discarded as counterpart to the BNS merger (Song et al. 2019; Paterson et al. 2021).

Our study of the theoretically predicted properties of the BNS population in their host galaxies shows that there is a significant bias towards detecting events in large galaxies with respect to the smaller ones. More specifically, for nearby BNS mergers which are GW-triggered, the probability of detecting an afterglow from a galaxy in the interval range $8 < \log[\mathcal{M}_{\rm gal,1}/{\rm M}_\odot] < 8.75$ is suppressed by about a factor of two with respect to BNS mergers in galaxies of mass within $10.25 < \log[\mathcal{M}_{\rm gal,1}/{\rm M}_\odot] < 11$. Since afterglow detections are key to host identification, this bias needs to be accounted for when extracting physical information on the underlying distribution of BNS mergers.

In addition to the snapshot at $z = 0.01$, which is well within the LIGO–Virgo current horizon, we studied the properties of the BNS population and its detectable counterparts also at the two higher redshift snapshots from TNG50 of $z = 0.1$ and $z = 1$. BNSs from a redshift distance $z = 1$ are beyond detection by current GW detectors, even at design sensitivity, but are expected to be detectable with the future *Einstein Telescope* (Punturo et al. 2010) and the Cosmic Explorer (Dwyer et al. 2015). On the other hand, BNS mergers occurring at $z \sim 0.1$, while beyond the horizon of the current instruments, will be within reach of LIGO and Virgo at design sensitivities,[5] and even more so with the addition of KAGRA and LIGO-India (Nissanke, Kasliwal & Georgieva 2013; for a comparison among detectors see e.g. fig. 1 of Yu et al. 2021).

For BNS mergers which are outside of the detectable GW horizon, detection relies on the observation of the gamma-rays emitted by the relativistic jet launched in association with the merger. These are the standard cosmological SGRBs (or at least a fraction of them, if a contribution is given also by NSBH mergers). The initial gamma-ray trigger is then used to search for the follow-up afterglow radiation. For a gamma-ray detection with the *Swift XRT* and *Fermi GBM* telescopes, we find that a GRB170817A-like event would need to be observed within a viewing angle from the jet axis of ∼29 deg at $z = 0.1$, and of ∼11 deg at $z = 1$. At these smaller viewing angles, the afterglow brightness ratio X-ray/O, but especially X-rays/R is larger than it is at larger viewing angles. As a result, a relatively larger fraction (compared with the GW-detected events) will be seen in X-rays than in optical, and even more so in radio.

It is interesting to compare our theoretical results with observations of cosmological SGRBs. As summarized in the review by Berger (2014), for SGRBs, the broadest and most homogeneous data set is in the X-ray band from the *Swift/XRT* satellite, with about 50 X-ray afterglow detections. Of these, about half have also optical afterglow detection, and only a handful do so also in radio. The broad consistency between our theoretical predictions and the broad-band observations of the cosmological SGRBs, having taken the jet properties of GRB170817A as 'canonical', provide yet another piece of evidence that indeed the bulk of the cosmological SGRB population is produced by GRB170817A-like events.

Looking into the future, while here we have made the first step in combining state-of-the art population synthesis calculations, galaxy simulations and numerical broad-band light curves to theoretically predict the observable properties of the SGRB population from GRB170817A-like BNS mergers events, there are several natural extensions of our study which we plan to address in future work. First is to consider a range in the intrinsic microphysical jet parameters. Since GRB170817A appears to be an average event compared to the bulk of SGRBs (Wu & MacFadyen 2019), we do not expect any quantitative change in the results, but there will be a spread in the luminosity brightness distributions. On the other hand, more significant changes can result from uncertainties intrinsic to the population synthesis modelling (see e.g. Broekgaarden et al. 2021 for a recent discussion on this topic).

An important extension of our work will be a similar study like the one we did here for field BNSs but for dynamically formed BNSs. It will then be interesting to compare statistically the EM predictions for the two populations, to see whether there are any telltale features which can help discriminate the two formation channels. Additionally, it will be useful a comparison with the EM properties of an NSBH merging population (albeit to date we are lacking an observationally derived prototype light curve such as for the case of GRB170817A) to help assess the fraction of SGRBs (if any) which is due to this interesting formation channel.

ACKNOWLEDGEMENTS

RP and YW gratefully acknowledge support by NSF award AST-2006839. MCA acknowledges financial support from the Austrian National Science Foundation through FWF stand-alone grant P31154-N27. MM and FS acknowledge financial support from the European Research Council for the ERC Consolidator grant DEMOBLACK, under contract no. 770017. DL acknowledges support from NASA grant NNX17AK42G (ATP) and NSF grant AST-1907955.

---

[4] We remark that this statement specifically refers to the probability of observing the broad-band EM counterpart to GW170817. On the other hand, the host galaxy of this event appears somewhat unusual (Palmese et al. 2017).

[5] https://dcc.ligo.org/LIGO-T1800133/public

Downloaded from https://academic.oup.com/mnras/article/512/2/2654/6547794 by libraryerms@stonybrook.edu user on 05 April 2022

DATA AVAILABILITY

All the simulation data produced for this paper will be made available upon request. The latest public version of the population synthesis code MOBSE can be downloaded from this repository. The IllustrisTNG simulations, including TNG50, are publicly available at this link.

REFERENCES

Abbott B. P. et al., 2016, Living Rev. Relativ., 19, 1
Abbott B. P. et al., 2017a, Phys. Rev. Lett., 119, 161101
Abbott B. P. et al., 2017b, Nature, 551, 85
Abbott B. P. et al., 2017c, ApJ, 848, L12
Abbott B. P. et al., 2020, ApJ, 892, L3
Adhikari S., Fishbach M., Holz D. E., Wechsler R. H., Fang Z., 2020, ApJ, 905, 21
Alexander K. D. et al., 2017, ApJ, 848, L21
Alexander K. D. et al., 2018, ApJ, 863, L18
Antonelli L. A. et al., 2009, A&A, 507, L45
Antonini F., Gieles M., 2020, MNRAS, 492, 2936
Antonini F., Rasio F. A., 2016, ApJ, 831, 187
Antonini F., Chatterjee S., Rodriguez C. L., Morscher M., Pattabiraman B., Kalogera V., Rasio F. A., 2016, ApJ, 816, 65
Arca Sedda M., 2020, ApJ, 891, 47
Arca Sedda M., Mapelli M., Spera M., Benacquista M., Giacobbo N., 2020, ApJ, 894, 133
Arcavi I. et al., 2017, Nature, 551, 64
Artale M. C., Mapelli M., Giacobbo N., Sabha N. B., Spera M., Santoliquido F., Bressan A., 2019, MNRAS, 487, 1675
Artale M. C., Mapelli M., Bouffanais Y., Giacobbo N., Pasquato M., Spera M., 2020a, MNRAS, 491, 3419
Artale M. C., Bouffanais Y., Mapelli M., Giacobbo N., Sabha N. B., Santoliquido F., Pasquato M., Spera M., 2020b, MNRAS, 495, 1841
Askar A., Szkudlarek M., Gondek-Rosińska D., Giersz M., Bulik T., 2017, MNRAS, 464, L36
Band D. et al., 1993, ApJ, 413, 281
Banerjee S., 2017, MNRAS, 467, 524
Banerjee S., 2021, MNRAS, 500, 3002
Banerjee S., Baumgardt H., Kroupa P., 2010, MNRAS, 402, 371
Bartos I., Kocsis B., Haiman Z., Márka S., 2017, ApJ, 835, 165
Belczynski K., Kalogera V., Bulik T., 2002, ApJ, 572, 407
Belczynski K., Perna R., Bulik T., Kalogera V., Ivanova N., Lamb D. Q., 2006, ApJ, 648, 1110
Belczynski K., Taam R. E., Kalogera V., Rasio F. A., Bulik T., 2007, ApJ, 662, 504
Belczynski K., Holz D. E., Bulik T., O'Shaughnessy R., 2016, Nature, 534, 512
Belczynski K., Ryu T., Perna R., Berti E., Tanaka T. L., Bulik T., 2017, MNRAS, 471, 4702
Belczynski K. et al., 2018, A&A, 615, A91
Beniamini P., Piran T., 2016, MNRAS, 456, 4089
Beniamini P., Piran T., 2019, MNRAS, 487, 4847
Beniamini P., Petropoulou M., Barniol Duran R., Giannios D., 2019, MNRAS, 483, 840
Beniamini P., Granot J., Gill R., 2020, MNRAS, 493, 3521
Berger E., 2010, ApJ, 722, 1946
Berger E., 2014, ARA&A, 52, 43
Bhat P. N. et al., 2016, VizieR Online Data Catalog, J/ApJS/223/28
Bloom J. S., 2003, PASP, 115, 271
Bloom J. S., Sigurdsson S., Pols O. R., 1999, MNRAS, 305, 763
Briel M. M., Eldridge J. J., Stanway E. R., Stevance H. F., Chrimes A. A., 2021, preprint (arXiv:2111.08124)
Broekgaarden F. S. et al., 2021, preprint (arXiv:2112.05763)
Camelio G., Dietrich T., Rosswog S., Haskell B., 2021, Phys. Rev. D, 103, 063014
Cao L., Lu Y., Zhao Y., 2018, MNRAS, 474, 4997
Chornock R. et al., 2017, ApJ, 848, L19
Chruslinska M., Belczynski K., Klencki J., Benacquista M., 2018, MNRAS, 474, 2937
Chruslinska M., Nelemans G., Belczynski K., 2019, MNRAS, 482, 5012
Chu Q., Yu S., Lu Y., 2022, MNRAS, 509, 1557
Ciolfi R., Kastaun W., Giacomazzo B., Endrizzi A., Siegel D. M., Perna R., 2017, Phys. Rev. D, 95, 063016
Coulter D. A. et al., 2017, Science, 358, 1556
Covino S. et al., 2006, A&A, 447, L5
Cowperthwaite P. S. et al., 2017, ApJ, 848, L17
D'Avanzo P. et al., 2009, A&A, 498, 711
de Mink S. E., Mandel I., 2016, MNRAS, 460, 3545
Di Carlo U. N., Giacobbo N., Mapelli M., Pasquato M., Spera M., Wang L., Haardt F., 2019, MNRAS, 487, 2947
Di Carlo U. N., Mapelli M., Bouffanais Y., Giacobbo N., Santoliquido F., Bressan A., Spera M., Haardt F., 2020a, MNRAS, 497, 1043
Di Carlo U. N. et al., 2020b, MNRAS, 498, 495
Dobie D. et al., 2018, ApJ, 858, L15
Dominik M., Belczynski K., Fryer C., Holz D. E., Berti E., Bulik T., Mandel I., O'Shaughnessy R., 2012, ApJ, 759, 52
Dominik M., Belczynski K., Fryer C., Holz D. E., Berti E., Bulik T., Mandel I., O'Shaughnessy R., 2013, ApJ, 779, 72
Downing J. M. B., Benacquista M. J., Giersz M., Spurzem R., 2010, MNRAS, 407, 1946
Drout M. R. et al., 2017, Science, 358, 1570
Dwyer S., Sigg D., Ballmer S. W., Barsotti L., Mavalvala N., Evans M., 2015, Phys. Rev. D, 91, 082001
Eldridge J. J., Stanway E. R., 2016, MNRAS, 462, 3302
Fan Y. Z., Zhang B., Kobayashi S., Mészáros P., 2005, ApJ, 628, 867
Fletcher C., Fermi-GBM Team, GBM-LIGO/Virgo Group, 2019, GCN Circ., 24185, 1
Fong W., Berger E., 2013, ApJ, 776, 18
Fong W., Berger E., Margutti R., Zauderer B. A., 2015, ApJ, 815, 102
Foucart F., Duez M., Gudinas A., Hébert F., Kidder L., Pfeiffer H., Scheel M., 2019, Phys. Rev. D, 100, 104048
Fragione G., Loeb A., 2019, MNRAS, 486, 4443
Fragione G., Silk J., 2020, MNRAS, 498, 4591
Fragione G., Grishin E., Leigh N. W. C., Perets H. B., Perna R., 2019a, MNRAS, 488, 47
Fragione G., Leigh N. W. C., Perna R., 2019b, MNRAS, 488, 2825
Fryxell B. et al., 2000, ApJS, 131, 273
Genel S., Bouché N., Naab T., Sternberg A., Genzel R., 2010, ApJ, 719, 229
Giacobbo N., Mapelli M., 2020, ApJ, 891, 141
Giacobbo N., Mapelli M., Spera M., 2018, MNRAS, 474, 2959
Granot J., Panaitescu A., Kumar P., Woosley S. E., 2002, ApJ, 570, L61
Guetta D., Stella L., 2009, A&A, 498, 329
Haggard D., Nynka M., Ruan J. J., Kalogera V., Cenko S. B., Evans P., Kennea J. A., 2017, ApJ, 848, L25
Hallinan G. et al., 2017, Science, 358, 1579
Hobbs G., Lorimer D. R., Lyne A. G., Kramer M., 2005, MNRAS, 360, 974
Hurley J. R., Tout C. A., Pols O. R., 2002, MNRAS, 329, 897
Kasen D., Metzger B., Barnes J., Quataert E., Ramirez-Ruiz E., 2017, Nature, 551, 80
Kasliwal M. M. et al., 2017, Science, 358, 1559
Kawamura T., Giacomazzo B., Kastaun W., Ciolfi R., Endrizzi A., Baiotti L., Perna R., 2016, Phys. Rev. D, 94, 064012
Kiuchi K., Kyutoku K., Sekiguchi Y., Shibata M., 2018, Phys. Rev. D, 97, 124039
Kopač D. et al., 2012, MNRAS, 424, 2392
Kremer K. et al., 2020, ApJS, 247, 48
Kroupa P., 2001, MNRAS, 322, 231
Kumamoto J., Fujii M. S., Tanikawa A., 2019, MNRAS, 486, 3942
Lamb G. P. et al., 2019, ApJ, 870, L15
Lazzati D., López-Cámara D., Cantiello M., Morsony B. J., Perna R., Workman J. C., 2017, ApJ, 848, L6
Lazzati D., Perna R., Morsony B. J., Lopez-Camara D., Cantiello M., Ciolfi R., Giacomazzo B., Workman J. C., 2018, Phys. Rev. Lett., 120, 241103
Lyman J. D. et al., 2018, Nature Astron., 2, 751

Downloaded from https://academic.oup.com/mnras/article/512/2/2654/6547794 by libraryerms@stonybrook.edu user on 05 April 2022

McKernan B., Ford K. E. S., Lyra W., Perets H. B., 2012, MNRAS, 425, 460
McKernan B. et al., 2018, ApJ, 866, 66
Mandel I., Broekgaarden F. S., 2021, preprint (arXiv:2107.14239)
Mandhai S., Lamb G. P., Tanvir N. R., Bray J., Nixon C. J., Eyles-Ferris R. A. J., Levan A. J., Gompertz B. P., 2021, preprint (arXiv:2109.09714)
Mapelli M., 2016, MNRAS, 459, 3432
Mapelli M., Giacobbo N., 2018, MNRAS, 479, 4391
Mapelli M., Giacobbo N., Ripamonti E., Spera M., 2017, MNRAS, 472, 2422
Mapelli M., Giacobbo N., Toffano M., Ripamonti E., Bressan A., Spera M., Branchesi M., 2018, MNRAS, 481, 5324
Mapelli M., Giacobbo N., Santoliquido F., Artale M. C., 2019, MNRAS, 487, 2
Mapelli M. et al., 2021, MNRAS, 505, 339
Marchant P., Langer N., Podsiadlowski P., Tauris T. M., Moriya T. J., 2016, A&A, 588, A50
Margutti R. et al., 2012, ApJ, 756, 63
Margutti R. et al., 2017, ApJ, 848, L20
Margutti R. et al., 2018, ApJ, 856, L18
Marinacci F. et al., 2018, MNRAS, 480, 5113
Miller M. C., Lauburg V. M., 2009, ApJ, 692, 917
Moe M., Di Stefano R., 2017, ApJS, 230, 15
Moffett A. J. et al., 2016, MNRAS, 462, 4336
Mooley K. P. et al., 2018, Nature, 561, 355
Most E. R., Papenfort L. J., Rezzolla L., 2019, MNRAS, 490, 3588
Murguia-Berthier A. et al., 2021, ApJ, 919, 95
Naiman J. P. et al., 2018, MNRAS, 477, 1206
Nakar E., Gal-Yam A., Fox D. B., 2006, ApJ, 650, 281
Neijssel C. J. et al., 2019, MNRAS, 490, 3740
Nelson D. et al., 2018, MNRAS, 475, 624
Nelson D. et al., 2019a, Comput. Astrophys. Cosmol., 6, 2
Nelson D. et al., 2019b, MNRAS, 490, 3234
Nissanke S., Kasliwal M., Georgieva A., 2013, ApJ, 767, 124
O'Leary R. M., Rasio F. A., Fregeau J. M., Ivanova N., O'Shaughnessy R., 2006, ApJ, 637, 937
O'Shaughnessy R., Belczynski K., Kalogera V., 2008, ApJ, 675, 566
O'Shaughnessy R., Kalogera V., Belczynski K., 2010, ApJ, 716, 615
Palmese A. et al., 2017, ApJ, 849, L34
Palmese A. et al., 2020, ApJ, 900, L33
Panaitescu A., Kumar P., 2000, ApJ, 543, 66
Paterson K. et al., 2021, ApJ, 912, 128
Perets H. B., Beniamini P., 2021, MNRAS, 503, 5997
Perna R., Belczynski K., 2002, ApJ, 570, 252
Perna R., Lazzati D., Fiore F., 2003, ApJ, 585, 775
Perna R., Wang Y.-H., Farr W. M., Leigh N., Cantiello M., 2019, ApJ, 878, L1
Perna R., Lazzati D., Cantiello M., 2021a, ApJ, 906, L7
Perna R., Tagawa H., Haiman Z., Bartos I., 2021b, ApJ, 915, 10
Pian E. et al., 2017, Nature, 551, 67
Pillepich A. et al., 2018a, MNRAS, 473, 4077
Pillepich A. et al., 2018b, MNRAS, 475, 648
Pillepich A. et al., 2019, MNRAS, 490, 3196
Piranomonte S. et al., 2008, A&A, 491, 183
Piro L. et al., 2019, MNRAS, 483, 1912
Podsiadlowski P., Langer N., Poelarends A. J. T., Rappaport S., Heger A., Pfahl E., 2004, ApJ, 612, 1044
Portegies Zwart S. F., McMillan S. L. W., 2000, ApJ, 528, L17
Portegies Zwart S. F., Yungelson L. R., 1998, A&A, 332, 173
Punturo M. et al., 2010, Class. Quantum Gravity, 27, 194002
Radice D., 2017, ApJ, 838, L2
Rasskazov A., Kocsis B., 2019, ApJ, 881, 20
Rastello S., Mapelli M., Di Carlo U. N., Giacobbo N., Santoliquido F., Spera M., Ballone A., 2020, MNRAS, 497, 1563
Resmi L. et al., 2018, ApJ, 867, 57
Rodriguez C. L., Loeb A., 2018, ApJ, 866, L5
Rodriguez C. L., Morscher M., Pattabiraman B., Chatterjee S., Haster C.-J., Rasio F. A., 2015, Phys. Rev. Lett., 115, 051101
Rodriguez C. L., Chatterjee S., Rasio F. A., 2016, Phys. Rev. D, 93, 084029
Rodriguez-Gomez V. et al., 2015, MNRAS, 449, 49
Rose J. C., Torrey P., Lee K. H., Bartos I., 2021, ApJ, 909, 207
Rossi E. M., Lazzati D., Salmonson J. D., Ghisellini G., 2004, MNRAS, 354, 86
Ruan J. J., Nynka M., Haggard D., Kalogera V., Evans P., 2018, ApJ, 853, L4
Ruiz M., Tsokaros A., Shapiro S. L., 2020, Phys. Rev. D, 101, 064042
Sakamoto T. et al., 2019, GCN Circ., 24184, 1
Salafia O. S., Ghirlanda G., Ascenzi S., Ghisellini G., 2019, A&A, 628, A18
Saleem M., Resmi L., Misra K., Pai A., Arun K. G., 2018, MNRAS, 474, 5340
Samsing J., 2018, Phys. Rev. D, 97, 103014
Samsing J., MacLeod M., Ramirez-Ruiz E., 2014, ApJ, 784, 71
Sana H. et al., 2012, Science, 337, 444
Santoliquido F., Mapelli M., Bouffanais Y., Giacobbo N., Di Carlo U. N., Rastello S., Artale M. C., Ballone A., 2020, ApJ, 898, 152
Santoliquido F., Mapelli M., Giacobbo N., Bouffanais Y., Artale M. C., 2021, MNRAS, 502, 4877
Sari R., Piran T., Narayan R., 1998, ApJ, 497, L17
Schaye J. et al., 2015, MNRAS, 446, 521
Schutz B. F., 2011, Class. Quantum Gravity, 28, 125023
Smartt S. J. et al., 2017, Nature, 551, 75
Soares-Santos M. et al., 2017, ApJ, 848, L16
Song H.-R., Ai S.-K., Wang M.-H., Xing N., Gao H., Zhang B., 2019, ApJ, 881, L40
Spera M., Mapelli M., Giacobbo N., Trani A. A., Bressan A., Costa G., 2019, MNRAS, 485, 889
Springel V. et al., 2018, MNRAS, 475, 676
Stevenson S., Berry C. P. L., Mandel I., 2017, MNRAS, 471, 2801
Stone N. C., Metzger B. D., Haiman Z., 2017, MNRAS, 464, 946
Tagawa H., Haiman Z., Kocsis B., 2020a, ApJ, 892, 36
Tagawa H., Haiman Z., Kocsis B., 2020b, ApJ, 898, 25
Tagawa H., Kocsis B., Haiman Z., Bartos I., Omukai K., Samsing J., 2021a, ApJ, 907, L20
Tagawa H., Kocsis B., Haiman Z., Bartos I., Omukai K., Samsing J., 2021b, ApJ, 908, 194
Tang P. N., Eldridge J. J., Stanway E. R., Bray J. C., 2020, MNRAS, 493, L6
Tanikawa A., Susa H., Yoshida T., Trani A. A., Kinugawa T., 2021, ApJ, 910, 30
Tanvir N. R. et al., 2017, ApJ, 848, L27
Troja E. et al., 2017, Nature, 551, 71
Tutukov A., Yungelson L., 1973, Nauchnye Informatsii, 27, 70
Vigna-Gómez A. et al., 2018, MNRAS, 481, 4009
Vogelsberger M., Genel S., Sijacki D., Torrey P., Springel V., Hernquist L., 2013, MNRAS, 436, 3031
Voss R., Tauris T. M., 2003, MNRAS, 342, 1169
Wu Y., MacFadyen A., 2019, ApJ, 880, L23
Yang Y. et al., 2019a, Phys. Rev. Lett., 123, 181101
Yang Y., Bartos I., Haiman Z., Kocsis B., Márka Z., Stone N. C., Márka S., 2019b, ApJ, 876, 122
Yu J. et al., 2021, ApJ, 916, 54
Zevin M., Samsing J., Rodriguez C., Haster C.-J., Ramirez-Ruiz E., 2019, ApJ, 871, 91
Zhu J.-P., Zhang B., Yu Y.-W., Gao H., 2021, ApJ, 906, L11
Ziosi B. M., Mapelli M., Branchesi M., Tormen G., 2014, MNRAS, 441, 3703

This paper has been typeset from a TEX/LATEX file prepared by the author.

Downloaded from https://academic.oup.com/mnras/article/512/2/2654/6547794 by libraryerms@stonybrook.edu user on 05 April 2022